CHALMERS
UNIVERSITY OF TECHNOLOGY

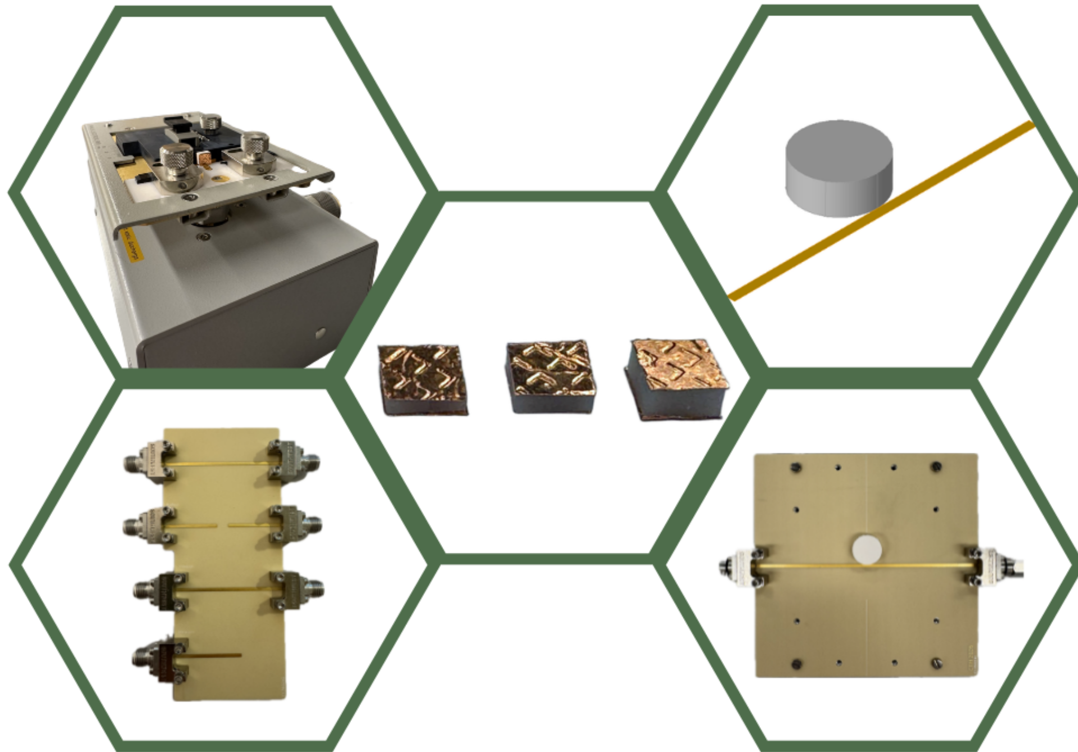

Dielectric Characterisation Methods for Additively Manufactured Ceramic Materials

Master's Thesis in Wireless, Photonics, and Space Engineering

EMMA ÖDMAN

DEPARTMENT OF MICROTECHNOLOGY AND NANOSCIENCE
CHALMERS UNIVERSITY OF TECHNOLOGY
Gothenburg, Sweden 2026
www.chalmers.se

Master's thesis 2026

Dielectric Characterisation Methods for Additively Manufactured Ceramic Materials

EMMA ÖDMAN

Department of Microtechnology and Nanoscience
Division of Microwave Electronics Laboratory
Chalmers University of Technology
Gothenburg, Sweden 2026

Dielectric Characterisation Methods for Additively Manufactured Ceramic Materials
EMMA ÖDMAN

© EMMA ÖDMAN, 2026.

Supervisor: Mattias Thorsell, Saab Surveillance
Examiner: Dan Kuylenstierna, Department of Microtechnology and Nanoscience

Master's Thesis 2026
Department of Microtechnology and Nanoscience
Division of Microwave Electronics Laboratory
Chalmers University of Technology
SE-412 96 Gothenburg
Telephone +46 31 772 1000

Cover: Samples and methods used for characterisation.

Typeset in LaTeX
Printed by Chalmers Reproservice
Gothenburg, Sweden 2026

Dielectric Characterisation Methods for Additively Manufactured Ceramic Materials
EMMA ÖDMAN
Department of Microtechnology and Nanoscience
Chalmers University of Technology

Abstract

Additive manufacturing has recently emerged as a promising technique for fabricating microwave components with complex geometries that are difficult or costly to achieve using conventional manufacturing methods. By enabling greater geometric freedom, additive manufacturing has the potential to improve component performance, reduce device size, and lower fabrication costs. However, to evaluate the suitability of additive manufacturing for high-frequency applications, it is essential to characterise how the fabrication process influences dielectric properties such as the relative permittivity and loss tangent.

This thesis, conducted in collaboration with Saab, focuses on the development and evaluation of dielectric characterisation methods for additively manufactured ceramics, as well as on investigating the influence of fabrication and post-processing on their performance. Three dielectric characterisation methods were developed and evaluated: a parallel plate capacitor method, a dielectric resonator method, and a broadband transmission line method. The parallel plate capacitor method was used to characterise samples in the green body, sintered, and hot isostatically pressed (HIPed) states.

Dielectric performance was found to be strongly dependent on material density, with a 0.6% increase in density corresponding to a 31.4% increase in relative permittivity and a 15.4% reduction in loss tangent. The relative permittivity remained stable over the temperature range 25 °C to 100 °C, varying by less than 2%, whereas the loss tangent increased by approximately 250%. In addition, the dielectric properties of the sintered and HIPed samples deviated from the manufacturer's specifications, highlighting a significant influence of the fabrication process on the final dielectric performance.

The findings demonstrate the importance of process optimisation in additive manufacturing of microwave ceramics and provide practical dielectric characterisation methods for evaluating and comparing fabrication parameters. The work contributes to the understanding of how additive manufacturing and post-processing influence the dielectric properties of ceramic materials intended for microwave applications.

Keywords: Additive Manufacturing, Ceramic Materials, Alumina, Dielectric Characterisation, Relative Permittivity, Loss Tangent, Microwave Materials, Hot Isostatic Pressing.

Acknowledgements

Writing this thesis has been an incredibly educational, rewarding, and at times challenging experience. Over the past six months, I have had the privilege of working alongside many talented colleagues, whose expertise and curiosity have really inspired me. I am very grateful for the opportunity to spend my time both at the Microwave Electronics Laboratory at Chalmers, as well as Saab.

I would like to express my gratitude to my supervisor, Mattias Thorsell, and examiner, Dan Kuylenstierna, for their engagement and willingness to answer questions throughout the project. Their support has been greatly appreciated.

A big thank you to Gabriele Muraca as well, for excellent collaboration and for providing invaluable assistance with the 3D printing work. I would also like to express my gratitude to everyone involved in ”Multi-Material Additive Manufacturing for Smart and Light-Weight Airborne Radar and EW Systems”, as well as Lithoz, for the additive manufacturing material, and Quintus, for the hot isostatic pressing of the samples.

And finally, thank you to all my friends and family. You are greatly appreciated!

Emma Ödman, Gothenburg, June 2026

List of Acronyms

Below is the list of acronyms that have been used throughout this thesis listed in alphabetical order:

AM	Additive Manufacturing
FEM	Finite Element Method
HIP	Hot Isostatic Pressing
LCM	Lithography-based Ceramic Manufacturing
SLA	Stereolithography
VNA	Vector Network Analyser

Contents

List of Acronyms **ix**

List of Figures **xiii**

List of Tables **xv**

1 Introduction **1**
- 1.1 Additive manufacturing . . . 1
  - 1.1.1 Fabrication of dielectric components . . . 2
- 1.2 Measurement of material properties . . . 3
- 1.3 Thesis scope and overview . . . 4

2 Theory **5**
- 2.1 Dielectric material . . . 5
- 2.2 Dielectric resonators . . . 7
- 2.3 Ceramic material properties . . . 10
- 2.4 Microwave measurements . . . 11
- 2.5 Parallel plate capacitor . . . 13
- 2.6 Dielectric resonator coupled to a microstrip line . . . 13
- 2.7 Multiline method . . . 14

3 Ceramic Additive Manufacturing **19**
- 3.1 Hot Isostatic Pressing . . . 21

4 Method **25**
- 4.1 Parallel plate capacitor . . . 25
  - 4.1.1 Measurement setup . . . 25
  - 4.1.2 Extraction of dielectric properties . . . 27
- 4.2 Resonator coupled to microstrip line . . . 28
  - 4.2.1 Measurement setup . . . 28
  - 4.2.2 Simulation setup . . . 30
  - 4.2.3 Extraction of dielectric properties . . . 31
- 4.3 Multiline method . . . 33
  - 4.3.1 Measurement setup . . . 33
  - 4.3.2 Simulation setup . . . 33
  - 4.3.3 Extraction of dielectric properties . . . 33

5 Results **35**
5.1 Parallel plate capacitor measurements 35
5.2 Resonator coupled to microstrip line 40
5.3 Multiline method 44

6 Conclusion **47**

Bibliography **49**

List of Figures

2.1 Magnetic field distribution for the first resonance mode of a cylindrical dielectric resonator with height L, radius r, and relative permittivity ε_r. Picture recreated with inspiration from [21] and [23]. 8

3.1 Temperature cycle for debinding the green body after fabrication. . . 20
3.2 Temperature for sintering the porous alumina component. 20
3.3 Temperature and pressure cycle for the HIP process at Quintus. . . . 22
3.4 Sintered and HIPed additively manufactured cubes, with densities presented in Table 3.2. Note that copper tape is attached to them in this figure, which was done after the density measurements. The dimensions are given in Table 4.1. 23

4.1 Measurement setup used for one-port S-parameter characterization of the parallel plate capacitor. (a) Overview of the setup consisting of a Keysight E5061B VNA, a Keysight 16201A 7 mm terminal adapter, and a Keysight 16192A parallel electrode SMD test fixture. (b) Close-up of the test fixture with the sample mounted. 25
4.2 Green body additively manufactured cubes, with dimensions presented in Table 4.1. Note that copper tape is attached to them in this figure, which was done after size measurements. 26
4.3 Measurement setup inside the ESPEC SH-242 temperature and humidity chamber. A phase-stable coaxial cable connects the test fixture to the VNA. 27
4.4 Setup for measuring a dielectric resonator coupled to a microstrip line. The measurements were performed with a Keysight N5247B PNA-X Network Analyser, two 2.4 mm coaxial cables, male to female 2.4 to 2.92 mm coaxial adapter, and a microstrip line designed to be 50 Ω at 11 GHz 29
4.5 TRL calibration kit with one line standard, designed to be 90° at 11 GHz with a frequency span of around 3 GHz to 19 GHz. The connectors are 2.92 Southwest SMA end launch connectors. 29
4.6 Substrate stackup in ADS used in the three-dimensional FEM simulations. The bottom layer is defined as the ground plane, the conductor copper, and the resonator a dielectric medium according to specifics. The MT40 substrate is defined from Eurocircuit datasheet. 30

4.7 Three-dimensional model of the measurement setup in ADS used for FEM simulations. In this example the radius of the resonator is 5 mm and the height 4 mm. The width of the microstrip line is 1.15 mm and the length 40 mm. 30

5.1 Relative permittivity of the additively manufactured cubes as a function of frequency. There is a clear increase in permittivity after HIP. . 35
5.2 Loss tangent of the additively manufactured cubes as a function of frequency, after linear regression. The loss tangent decreases after sintering. 36
5.3 The calculated relative permittivity and loss tangent of the additively manufactured cubes before and after HIP, without the use of a linear regression approximation. The permittivity and loss tangent seem to have a size dependence. 37
5.4 Linear regression of capacitance as a function of the area divided by height of the 3D printed cubes. The sintered, and sintered and HIPed cubes have a good linear fit compared to the green body cubes. . . . 38
5.5 Measurements of relative permittivity over temperature for sintered and HIPed cubes, compared with results from measuring outside of the temperature chamber. The discrepancy between outside and inside temperature chamber could be because of interference with the shielded chamber. The average relative permittivity varied by less than 2 % over the temperature span. 39
5.6 Measurements of loss tangent over temperature for sintered and HIPed cubes, compared with results from measuring outside of the temperature chamber. The loss increases with temperature. 40
5.7 Measured and simulated scattering parameters of a green body dielectric resonator coupled to a microstrip line. (a) Reflection coefficient, S_{11}. (b) Transmission coefficient, S_{21}. 41
5.8 Magnitude of the transmission of a microstrip line coupled to a DRT 10.5GHz resonator. The first resonance frequency is 11.15 GHz. . . . 41
5.9 S_{21}-parameters from FEM and schematic simulations with relative permittivity tuned in order to resonate at 11.15 GHz. 42
5.10 Close-up of the measured, schematic and FEM transmission around the first resonance frequency. 43
5.11 Resonant frequency as a function of relative permittivity for a cylindrical resonator with a diameter of 5.07 mm and height of 2.19 mm, calculated using numerical methods presented by Pozar [21], Itoh and Rudokas [27], and Konishi *et al* [26]. The specified permittivity and resonance frequency of the DRT 10.5 GHz resonator is also plotted. . 44
5.12 Relative permittivity and loss tangent calculated using the multiline method from measured and simulated S-parameters from two microstrip lines with a length difference of 4.14 mm. The dielectric loss was estimated taking conductor losses into account, but not accounting for surface roughness. 45

List of Tables

3.1 Material parameters of sintered high-purity LithaLox from Lithoz, containing high-purity aluminium oxide [47]. 21
3.2 Measured density and relative density of samples after sintering, before and after HIP. The density measurement was performed using the Archimedes principle and compared to the theoretical density in Table 3.1 22

4.1 Dimensions of 3D-printed cubes before and after processing. An image of the sintered and HIPed cubes are given in Figure 3.4 and the green body cubes in Figure 4.2. 26

5.1 Average relative density and dielectric properties of the printed alumina samples at different processing stages. 36
5.2 Coupling factor and unloaded quality factor obtained using the three-point method (Algorithm 2) and from the phase of the de-embedded characteristic impedance of the resonator (Algorithm 3). 43
5.3 Relative permittivity and loss tangent at 10 GHz from measurements and simulations compared to data sheet values for I-Tera MT40. . . . 44

1

Introduction

More than 130 years ago, Faraday introduced the term “dielectric” to describe a phenomenon similar to current flow in a capacitor [1], [2]. He suggested that current entering one plate appears to pass through the insulating material, enabling the opposite plate to become charged. This is because dielectrics are a type of electrical insulators that become polarised when exposed to an electric field [1]. Because of this property, dielectric materials have played an important role in modern electronics. They are key components in microwave filters, resonators, waveguides, and capacitors. However, the fabrication process can be costly and may limit implementation of new design concepts.

These limitations are particularly relevant in airborne sensing applications, where microwave components are essential. For example, modern airborne sensing systems face increasing demands for reduced size, weight, and power consumption while maintaining high performance. As smaller, faster-moving threats employing stealth technology emerge, there is a growing need to improve situational awareness in the air domain. This has created a demand for lightweight, compact, and high-efficiency sensors suitable for integration in small airborne platforms.

Meeting these requirements requires not only improved sensor designs but also more flexible and cost-effective manufacturing techniques. In particular, there is a growing interest in fabrication methods capable of producing components with complex, application-specific geometries that integrate both conductive and dielectric materials within a single structure. To address these challenges, alternative manufacturing methods are being explored. One promising approach is additive manufacturing (AM), also known as 3D printing. This method creates objects by joining materials, usually in a layer-by-layer approach. For example, additive manufacturing has been implemented in production of antennas, filters, diplexers and dielectric resonators [3]–[14].

1.1 Additive manufacturing

Several additive manufacturing processes exist. For ceramic materials, one of the most commercially established methods is vat photopolymerisation, particularly stereolithography (SLA) [15]. This is a 3D printing process where a container (vat) is filled with a liquid slurry, consisting of ceramics and polymers, and then selectively cured by light-activated polymerisation. Other methods include material jetting, in which droplets of build material are selectively deposited and cured with UV, and

fused deposition. The latter method works by heating a filament and dispensing it selectively through a nozzle [15]. These methods can also be used for other materials, such as polymers.

1.1.1 Fabrication of dielectric components

Conventionally, polymers have been the primary materials used in 3D printing. However, as additive manufacturing expands into electrical and electromagnetic applications, alternative materials are being explored. Among these, ceramics have gained increasing attention due to their favourable thermal and dielectric properties.

Multiple techniques are available for producing microwave components using additive manufacturing. These include printing polymer structures followed by metallisation, directly printing metallic components, or fabricating components using ceramic materials. The main benefits of using AM techniques compared to conventional methods is the freedom of design and cost-effectiveness in small-to-medium volume. Since the principle of printing the material builds on a layer-by-layer approach, the limitation lies in the allowed printing size and amount of material used. Another benefit of 3D printing is the reduction in weight. In [6], Guo *et al.* print a plastic filter structure based on spherical resonators using stereolithography and coat it with a thin layer of copper. This lowers the weight from 2 kg using traditional milling to 0.28 kg. However, their filter is limited by the working temperature that can go no higher than 39−46 °C. To address this limitation, a ceramic material can be chosen instead.

Using lithography-based ceramic manufacturing (LCM), Miek *et al.* [5] present a monolithic 3D-printed ceramic X-shaped dual-mode microwave filter. Because of the fabrication process, there are no alignment issues, even though there are complex geometries inside. When designing the filter, they estimate an initial ceramic permittivity of 9.4. In order to achieve more accurate results, they perform material characterisation on the 3D printed alumina by measuring a resonator excited in a cavity. The resulting S-parameters are then matched to simulation in order to find a permittivity of 9.32 at 5.27 GHz. The final filter had a significant bandwidth reduction when compared to simulations due to a decreased inter-cavity coupling. This effect could be caused by deviations in the 3D printing process or unequal shrinkage during sintering.

As [6] and [5] highlight, there are many advantages to using additive manufacturing processes. The main benefit is the ability to create complex shapes. In [7]–[11], additive manufacturing is used to fabricate variants of waveguide bandpass filters through structural deformation, the introduction of inserts, and modifications to the conventional rectangular geometry. In these cases, the final product is either fabricated in resin and coated in metal, or produced directly through metal additive manufacturing.

When 3D printing using ceramic materials, it is possible to create custom microstrip structures. In [12], they present at low-pass filter created by varying the substrate height and line width of a microstrip. This emphasizes the possibility of compact,

integrable filters. However, it also requires good knowledge of the manufactured material and its electrical properties. In [5], the measured permittivity differed slightly from the specified value, demonstrating that material properties can deviate after fabrication. As electromagnetic component performance is dependent on these properties, accurate characterisation methods are important for additively manufactured materials. With reliable characterisation techniques, it becomes possible to investigate the effects of different manufacturing processes, evaluate material combinations, and develop multi-material components with predictable dielectric behaviour.

1.2 Measurement of material properties

Two main categories of methods are commonly used for measuring dielectric properties – transmission–reflection methods, in which the scattering parameters are analysed, and resonant methods, where the dielectric properties are determined from the effect of the material under test on the resonant frequency of the system.

Deffenbaugh *et al.* [16] present three different methods for characterising 3D-printed materials fabricated using fused deposition modelling and stereolithography. The proposed methods include measurements using an LCR meter at 1 MHz and 2 MHz, where the capacitance is used to determine the relative permittivity and loss tangent, and measurements using an impedance analyser based on the same extraction principle. In addition, an X-band waveguide operating in the frequency range 8.2-11 GHz is utilized, where the dielectric properties are extracted from the effect of the material sample on the resonant behaviour of the system.

Another method is presented by Takach *et al.* [17] where they use a two-line coaxial cable technique in order to find the relative permittivity and loss tangent. This is done by measuring two coaxial lines with a well known length difference and comparing the results with and without the material under test. From the scattering parameters, the propagation constant can be found.

In [18], Goulas *et al.* investigate the impact of printer settings on the relative permittivity and loss tangent of composite thermoplastic filament, manufactured by fused deposition. The manufacturing properties investigated were extrusion width, layer height, and material infill. To do this, they placed printed samples in an X-band cavity and measured the transmission and reflection parameters. These scattering parameters were then used in the Nicolson–Ross–Weir (NRW) method to calculate the relative permittivity and loss tangent of the material. A similar approach was employed by Castles *et al.* [19] to validate results obtained using a split post dielectric resonator, which determines dielectric properties by analysing the influence of a sample on the resonant frequency. In their work, the permittivity of the printed material was controlled by varying the concentration of ceramic filler within the polymer during fused deposition modelling. Alimenti *et al.* [20] also characterise the loss tangent and relative permittivity of 3D printed plastic materials using a resonator based model, but this time with a modified Hakki-Coleman resonator. The device under test was photopolymer resonator discs printed using PolyJet deposition, a type of material jetting.

The resonator method is the most commonly used technique for characterising these materials, but it requires specialised measurement equipment. In addition, there is a lack of characterisation studies focused on ceramic materials, despite their potential advantages in terms of thermal stability and higher relative permittivity. For instance, the variation in relative permittivity reported by Miek *et al.* [5] may significantly influence the performance of the final component. This highlights the need for further investigation into the dielectric properties of 3D-printed ceramic materials, as well as the influence of printing and post-processing parameters on these properties. In order to appropriately implement additively manufactured components we have to understand how the fabrication parameters affect the performance of the material.

1.3 Thesis scope and overview

The purpose of this Master's thesis is to present methods for characterising additively manufactured ceramic material, as well as discuss the impact of fabrication processes on the dielectric properties. The material investigated is high-purity LithaLox alumina (Al_2O_3) from Lithoz, fabricated by lithography-based ceramic manufacturing (LCM). Some of the samples undergo post-processing by hot isostatic pressing (HIP). Three dielectric characterisation methods are presented and evaluated: a parallel plate capacitor method, a dielectric resonator method, and a broadband transmission line method. The parallel-plate capacitor method was used to characterise samples in the green body, sintered, and HIPed states. Preliminary findings indicate that the dielectric properties are tied to the density och the material. The highest relative permittivity and lowest loss tangent was observed in samples with the highest relative density.

The thesis is organised as follows. Section 2 introduces relevant theory about dielectric material and characterisation methods. Section 3 states how the 3D printed components were fabricated at Chalmers Centre for Additive Manufacturing, CAM2, and details how they were post-processed. Section 4 presents the experimental setup, materials, and tools used. Section 5 demonstrates and discusses the achieved results, and Section 6 concludes the thesis by summarising the findings.

2 Theory

This chapter aims to explain relevant theory regarding dielectric material and its uses, additive manufacturing, and measurement methods for dielectric material. An analysis of ceramic material properties and their impact on the dielectric properties is also conducted.

2.1 Dielectric material

A dielectric is an electrically insulating material that becomes polarised when exposed to an external electric field [1], [21]. Common dielectric materials include air, glass, ceramics, polymers, and water, each characterised by different polarisation mechanisms and dielectric properties. Unlike conductors, where electric charges can move freely through the material, charges in a dielectric only shift slightly from their normal positions, producing what is known as dielectric polarisation. This displacement generates an internal electric field that opposes and weakens the external field within the material.

The electric polarisation, denoted by $\bar{\mathbf{P}}_{\mathbf{e}}$, contributes to the electric flux density according to

$$\bar{\mathbf{D}} = \varepsilon_0 \bar{\mathbf{E}} + \bar{\mathbf{P}}_{\mathbf{e}} = \varepsilon \bar{\mathbf{E}}, \tag{2.1}$$

where ε is the complex permittivity of the medium [21],

$$\varepsilon = \varepsilon' - j\varepsilon'' = \varepsilon_0(\varepsilon_r' - j\varepsilon_r''). \tag{2.2}$$

ε_0 is the permittivity in vacuum and ε_r is the complex relative permittivity. The real part, ε', represents the material's ability to store electric energy. A higher relative permittivity means the material becomes polarized more easily when an electric field is applied. The imaginary part, ε'', represents dielectric losses in the material due to damping of the vibration dipole moments.

The dielectric loss is commonly quantified using the loss tangent,

$$\tan\delta = \frac{\varepsilon''}{\varepsilon'}, \tag{2.3}$$

which is defined as the ratio between the dissipated and stored electromagnetic energy in the dielectric medium.

The dielectric properties of a material directly influence electromagnetic wave propagation through the medium. In particular, the permittivity determines the phase velocity, wavelength, and attenuation of propagating fields, as described by Maxwell's equations. They are given by

$$\begin{aligned} \nabla \times \bar{\mathbf{E}} &= \frac{-\partial \bar{\mathbf{B}}}{\partial t} - \bar{\mathbf{M}} \\ \nabla \times \bar{\mathbf{H}} &= \frac{\partial \bar{\mathbf{D}}}{\partial t} + \bar{\mathbf{J}} \\ \nabla \cdot \bar{\mathbf{D}} &= \rho \\ \nabla \cdot \bar{\mathbf{B}} &= 0 \end{aligned} \tag{2.4}$$

where $\bar{\mathbf{E}}$ is the electric field, $\bar{\mathbf{B}}$ the (fictitious) magnetic flux density, $\bar{\mathbf{M}}$ the magnetic current density, $\bar{\mathbf{H}}$ the magnetic field, $\bar{\mathbf{D}}$ the electric flux density, and $\bar{\mathbf{J}}$ the electric current density [21]. In a source-free, linear, isotropic, homogenous region, we can write Maxwell's first two equations as

$$\begin{aligned} \nabla \times \bar{\mathbf{E}} &= -j\omega\mu\bar{\mathbf{H}} \\ \nabla \times \bar{\mathbf{H}} &= j\omega\varepsilon\bar{\mathbf{E}} \end{aligned} \tag{2.5}$$

given that $\bar{\mathbf{B}} = \mu\bar{\mathbf{H}}$, where μ is the complex permeability of the medium. The permeability relates to the magnetic polarization of the medium, and is analogous to the permittivity. From this, we can derive the Helmholtz equation for a general lossy medium in terms of $\bar{\mathbf{E}}$ as

$$\nabla^2\bar{\mathbf{E}} - \gamma^2\bar{\mathbf{E}} = 0, \tag{2.6}$$

where the complex propagation constant γ is given by

$$\begin{aligned} \gamma &= \alpha + j\beta \\ &= j\omega\sqrt{\mu\varepsilon}\sqrt{1 - j\frac{\sigma}{\omega\varepsilon}}. \end{aligned} \tag{2.7}$$

σ is the conductivity of the material, α is called the attenuation constant, and β the phase constant. The wavelength is related to the phase constant as

$$\lambda = \frac{2\pi}{\beta}. \tag{2.8}$$

The skin depth, the distance before a field decays by $\frac{1}{e}$, is related to the attenuation constant as

$$\delta_s = \frac{1}{\alpha}. \tag{2.9}$$

For an ideal dielectric, $\sigma = 0$ and μ and ε are real quantities. The propagation constant is then purely imaginary and reduced to $\gamma = j\beta$.

2.2 Dielectric resonators

The dielectric resonator was first introduced by Richtmyer in 1939 [22], where he showed that dielectrics could be used as high frequency oscillators. Since then they have become important components in modern electronic devices, used in antennas and filters. Electrical resonators are designed to achieve standing wave behaviour at specific resonance frequencies. This can be accomplished through various designs; series and parallel resonance circuits, transmission line resonators, cavity resonators, and dielectric resonators [21].

Dielectric resonators confine the electromagnetic field, except for an exponentially decreasing part outside [21], [22]. In order to quantify the frequency selectivity of the resonator, we can look at the quality factor

$$Q = \omega \frac{\text{average energy stored}}{\text{energy loss/second}}. \tag{2.10}$$

The Q-factor can be denoted as the loaded, unloaded, and external quality factor depending on how it is measured. The unloaded quality factor, Q_0, excludes external loading effects and is the Q of the resonator itself [21]. As the resonator couples to other circuitry, the impact is described through the external quality factor Q_{ex}. What is measured in practice is a combination of both the external and unloaded quality factor,

$$\frac{1}{\mathrm{Q}_L} = \frac{1}{\mathrm{Q}_0} + \frac{1}{\mathrm{Q}_{\mathrm{ex}}} \tag{2.11}$$

where Q_L is the loaded quality factor [21].

The geometry of the dielectric resonator, as well as its intrinsic properties, decides at what frequencies there is resonance. If we consider a cylindrical dielectric resonator with height L, radius r, and relative permittivity ε_r, the magnetic field distribution for the first resonance mode is shown in Figure 2.1. The evanescent behaviour outside of the resonator is due to high permittivity of the resonator (in the range of 10-100) in comparison to air.

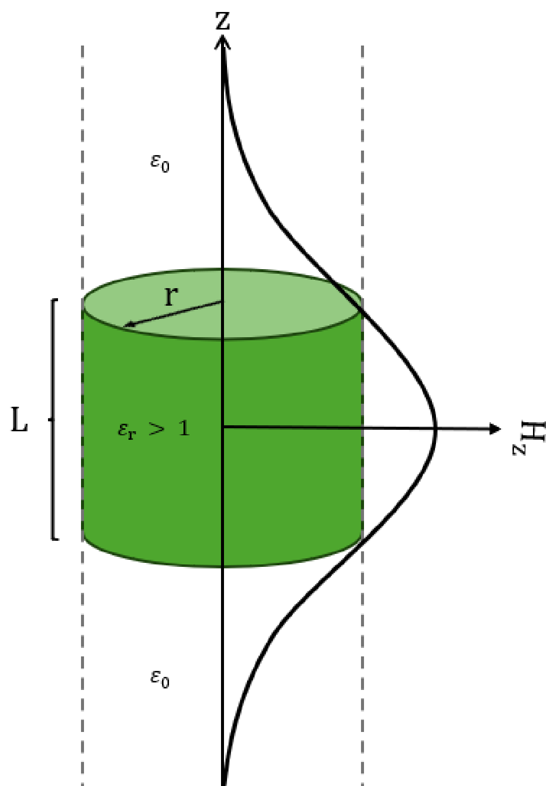

Figure 2.1: Magnetic field distribution for the first resonance mode of a cylindrical dielectric resonator with height L, radius r, and relative permittivity ε_r. Picture recreated with inspiration from [21] and [23].

In this waveguide the lowest order mode is $\text{TE}_{01\delta}$, where $\delta = \frac{2L}{\lambda_g} < 1$ denotes the z variation of the resonant mode [21]. This is because the resonant length is smaller than $\frac{\lambda_g}{2}$, where λ_g is the guide wavelength of the TE_{01} mode.

In order to approximate the resonant frequencies we can follow the analysis presented by Pozar [21], which in turn follows that of Cohn [24]. Assume that we have a magnetic wall boundary condition at $\rho = r$ [21],[25]. For TE modes in the dielectric waveguide, $E_z = 0$ and H_z must satisfy the wave equation

$$(\Delta^2 + k^2)H_z = 0 \tag{2.12}$$

where

$$k = \begin{cases} \sqrt{\varepsilon_r}k_0 & |z| < L/2 \\ k_0 & |z| > L/2 \end{cases}$$

Under the condition that H_z is finite at $\rho = 0$ and zero at $\rho = r$, $\frac{\partial}{\partial\phi} = 0$, and $k_c^2 = k^2 - \beta^2$ can write an expression for H_z as

$$H_z = H_0 J_0(k_c\rho)e^{\pm j\beta z}. \tag{2.13}$$

J_0 is the Bessel function of the first kind as a function of k_c and ρ. In this case, we can write $k_c = \frac{p_{01}}{r}$ with $p_{01} = 2.405$.

Inside the waveguide ($|z| < L/2$) we have a real propagation constant $\beta = \sqrt{\varepsilon_r k_0^2 - k_c^2}$, and in the air region outside the resonator ($|z| > L/2$) the propagation is imaginary and given by $\alpha = \sqrt{k_c^2 - k_0^2}$. We now want to match the transverse fields at $z = \pm L/2$, where we have the field expressions given by

$$E_\phi = \begin{cases} A J_0'(k_c\rho)\cos\beta z & |z| < L/2 \\ B J_0'(k_c\rho)e^{-\alpha|z|} & |z| > L/2 \end{cases} \tag{2.14}$$

and

$$H_\rho = \begin{cases} -\frac{jA}{Z_d} J_0'(k_c\rho)\sin\beta z & |z| < L/2 \\ \pm\frac{B}{Z_a} J_0'(k_c\rho)e^{-\alpha|z|} & |z| > L/2 \end{cases} \tag{2.15}$$

where A, B are unknown amplitude coefficients, $Z_d = \frac{\omega\mu_0}{\beta}$, and $Z_a = \frac{j\omega\mu_0}{\alpha}$.
This leads to the simplified transcendental equation

$$\tan\frac{\beta L}{2} = \frac{\alpha}{\beta} \tag{2.16}$$

which can be numerically solved for $k_0 = \frac{2\pi f_0}{c}$ in order to find the resonant frequency.

Using this method, we do not take fringing fields into account. This means that we have an error of about 10%. However, if the resonator faces metal plates at a shorter distance, the magnetic wall approximation is quite valid [26]. In order to get more accurate results, we can use the method proposed by Itoh and Rudokas [27]. In the paper they compare the field expression for a cylindrical dielectric resonator on a substrate by dividing the field expression into different regions and look at the boundary conditions. This yields a coupled eigenvalue equation

$$\frac{J_0'(hr)}{hJ_0(hr)} + \frac{K_0'(pr)}{pK_0(pr)} = 0 \tag{2.17a}$$

$$\beta L = q\pi + \tan^{-1}\left(\frac{\gamma}{\beta}\right) + \tan^{-1}\left(\frac{\xi}{\beta}\coth\xi t\right) \tag{2.17b}$$

where $q = 0, 1, 2, \ldots$ and

$$\begin{aligned} \beta^2 &= \varepsilon_{r1}k_0^2 - h^2 = k_0^2 + p^2, \\ \gamma^2 &= h^2 - k_0^2, \\ \xi^2 &= h^2 - \varepsilon_{r2}k_0^2. \end{aligned}$$

ε_{r1} denotes the relative permittivity of the dielectric resonator, and ε_{r2} the relative permittivity of the substrate. If we let $\varepsilon_{r2} = 1$ and $t \to \infty$, Equation 2.17b simplifies to the transcendental Equation 2.16 for $q = 0$. This method, however, does not work as well for resonators with a lower ε_r. Instead we can use the variational method from Konishi *et al.* [26], which is valid when the resonator is placed in free space or far from ground. Their method starts by calculating ω_0 using the same set of equations presented by Pozar [21] and then adding a correctional term $\frac{\Delta\omega}{\omega_0}$. Assuming we have found k_0 from Equation 2.16, we also have the values for β, α, k_c. Let

$$\begin{aligned} x_0 &= k_0 r \\ \xi &= \frac{L}{2r} \\ \eta &= \frac{\alpha}{\beta} + \frac{\beta L}{2} \cdot \left(1 + \frac{\alpha^2}{\beta^2}\right) \end{aligned}$$

and define

$$\begin{aligned} \frac{\Delta\omega}{\omega_0} &= F(\alpha, \beta, x_0, \xi, \varepsilon_r) \\ &= \frac{-2a(\beta + \alpha\eta) \int_{-\infty}^{\infty} \sqrt{x_0^2 - x^2}\, \dfrac{H_0^{(2)}\left(\sqrt{x_0^2 - x^2}\right)}{H_1^{(2)}\left(\sqrt{x_0^2 - x^2}\right)} A^2 \, dx}{\pi \alpha a x_0^2 \varepsilon_r \eta \left[\xi + \frac{\sin(2\beta a \xi)}{2\beta a} + \frac{\cos^2(\beta a \xi)}{\alpha a}\right]} \end{aligned} \tag{2.18}$$

where A is given by

$$\begin{aligned} A = \frac{r\beta \sin(r\beta\xi)\cos(x\xi)}{(r\beta)^2 - x^2} + \frac{r\alpha \cos(x\xi)\cos(r\beta\xi)}{(r\alpha)^2 + x^2} - \\ - x \sin(x\xi)\cos(r\beta\xi) \cdot \frac{(r\beta)^2 + (r\alpha)^2}{\left((r\beta)^2 - x^2\right)\left((r\alpha)^2 + x^2\right)}. \end{aligned} \tag{2.19}$$

From the results presented in [26], the error between theoretical and experimental results was less than one percent.

2.3 Ceramic material properties

The relative permittivity, loss tangent, and temperature stability, are important parameters used to characterise dielectric ceramics for use at radio frequencies. For a dielectric resonator, the size is inversely proportional to the square root of the relative permittivity [28]. This means that we want the relative permittivity to be as high as possible while maintaining a low loss tangent and temperature stability.

The dielectric constant and loss are influenced by the material composition. For example, Penn *et al.* [29] studied the influence of grain size and porosity on the

dielectric properties of alumina. They showed that the loss is heavily dependent on the porosity of the material, where even small porosity led to an increase in loss. The dielectric constant was also affected by the porosity, showing a decrease as the porosity increased. For a 0.3 fractional porosity, the relative permittivity was 40 % lower than for a fully dense sample.

Jenkel *et al.* [30] also performed a similar study, but instead investigating the effects of sintering time on the dielectric properties of additively manufactured alumina. They found that the relative permittivity changed from 4.4 when sintering at 1250 °C to 9.2 at 1650 °C. Similarly, the quality factor increased with sintering temperature. This was attributed to the grain size and porosity of the samples, where the grain size increased and porosity decrease with sintering temperature.

2.4 Microwave measurements

For a travelling wave on a transmission line, the characteristic impedance Z_0 is defined by the ratio between the voltage and the current [21]. The complex impedance can be written as

$$Z = R + jX \tag{2.20}$$

where the real part R is related to the dissipated power and the imaginary part X relates to the net energy stored in the network.

For an arbitrary N-port microwave network, we can use the impedance matrix $[Z]$ to relate the voltages and currents as

$$\begin{bmatrix} V_1 \\ V_2 \\ \vdots \\ V_N \end{bmatrix} = \begin{bmatrix} Z_{11} & Z_{12} & \cdots & Z_{1N} \\ Z_{21} & & & \vdots \\ \vdots & & \ddots & \vdots \\ Z_{N1} & \cdots & \cdots & Z_{NN} \end{bmatrix} \begin{bmatrix} I_1 \\ I_2 \\ \vdots \\ I_N \end{bmatrix}. \tag{2.21}$$

The admittance matrix can similarly be derived as $[I] = [Y][V]$, meaning that $[Y] = [Z]^{-1}$. The matrix elements of $[Z]$ can be found by

$$Z_{ij} = \left.\frac{V_i}{I_j}\right|_{I_k=0 \text{ for } k\neq j}. \tag{2.22}$$

When dealing with high-frequency networks, it becomes a practical problem to measure voltages and current. A better way to characterise such a matrix would be with scattering parameters, which represent the incident, reflected, and transmitted waves. The scattering matrix, and its S-parameters, relates the incident voltage to the reflected voltage as

$$\begin{bmatrix} V_1^- \\ V_2^- \\ \vdots \\ V_N^- \end{bmatrix} = \begin{bmatrix} S_{11} & S_{12} & \cdots & S_{1N} \\ S_{21} & & & \vdots \\ \vdots & & \ddots & \\ S_{N1} & \cdots & & S_{NN} \end{bmatrix} \begin{bmatrix} V_1^+ \\ V_2^+ \\ \vdots \\ V_N^+ \end{bmatrix}. \tag{2.23}$$

A specific element can be determined as

$$S_{ij} = \left. \frac{V_i^-}{V_j^+} \right|_{V_k^+ = 0 \text{ for } k \neq j}. \tag{2.24}$$

We can write the scattering matrix in terms of the impedance matrix and identity matrix $[U]$ as

$$[S] = ([Z] + [U])^{-1} ([Z] - [U]) \tag{2.25}$$

which reduces to

$$S_{11} = \frac{Z_{11} - Z_0}{Z_{11} + Z_0} \tag{2.26}$$

for a one-port network with characteristic impedance Z_0.

Scattering parameters can be measured using a Vector Network Analyzer (VNA), which is a microwave measurement instrument designed to analyze the transmitted and reflected signals of a network [21]. In order to get accurate results, calibration of the VNA should be performed. By doing this, systematic errors are removed and the reference plane shifts from the VNA ports to the location where the calibration is conducted [31]. The calibration relies on calibration standards that are used to quantify and correct errors introduced by the VNA and test setup. The four most common standards are short (S), open (O), load (L), and through (T) [31]. The short standard represents a short circuit at the reference plane and is used for reflection calibration. The open standard represents an open circuit, typically with defined parasitic effects that become significant at higher frequencies. The load standard, also referred to as a match, consists of a termination matched to the characteristic impedance of the system in order to minimise reflections. Lastly, the through standard represents an ideal connection between two ports and is used for transmission calibration.

When even more accurate results are required and there are no calibration standards with the same connectors as the device under test (DUT), a TRL (Through, Reflect, Line) calibration can be performed [32]. The through standard can be either zero-length or non-zero length. The reflect standard can be anything with high reflection, but the phase must be known within a quarter of a wavelength. The line standard must have the same impedance and propagation constant as the through, but must be of a different length. A single line standard can be used over an 8:1 frequency range, and at each frequency the phase difference between through and line must

be greater than 20 degrees and less than 160 degrees. If a broader frequency span is required, several line standards can be used.

2.5 Parallel plate capacitor

Consider a parallel plate capacitor consisting of two metal plates with an area A, filled by a dielectric of uniform height h. The capacitance is then given by

$$C = \varepsilon_r \varepsilon_0 \frac{A}{h}, \tag{2.27}$$

where ε_0 is the permittivity in vacuum and ε_r is the relative permittivity of the dielectric [33]. The capacitance can also be described using a complex impedance $Z = R + jX$, where R is the resistance and X the reactance. The reactance can be either inductive, X_L, or capacitive, X_C. For the capacitive series reactance we have the relation,

$$X_C = -\frac{1}{\omega C}. \tag{2.28}$$

By letting $C_0 = \varepsilon_0 \frac{A}{h}$, we can combine Equation 2.27 and 2.28 to obtain an expression for ε_r,

$$\varepsilon_r = -\frac{1}{\omega X_C C_0}. \tag{2.29}$$

The quality of the reactance can be quantified using the loss tangent, tan δ, which is defined as

$$\tan \delta = -\frac{R}{X_C} \text{ [34]}. \tag{2.30}$$

Similarly, we can also use the admittance $Y = G + jB$, where G is the conductance and B the susceptance, to define the relative permittivity and loss tangent.

$$\begin{aligned} \varepsilon_r &= \frac{B}{\omega C_0}, \\ \tan \delta &= \frac{G}{B}. \end{aligned} \tag{2.31}$$

2.6 Dielectric resonator coupled to a microstrip line

When placing a dielectric resonator beside a microstrip line, they couple to each other. This effect can be used to realise oscillators and filters [35]. The coupling

factor, β, is defined as the ratio between the resonator coupled resistance R at the resonance frequency and the resistance external to the resonator,

$$\beta = \frac{R}{R_{\text{ext}}} = \frac{S_{11o}}{S_{21o}}, \tag{2.32}$$

where S_{11o} and S_{21o} are the real valued magnitudes at the resonant frequency [35]. The coupling factor relates to the quality factors as

$$Q_0 = Q_L(1+\beta) = \beta Q_{\text{ex}}. \tag{2.33}$$

We can find the loaded quality factor from the 3 dB bandwidth, Δf, and centre frequency,f_0, of the resonance as

$$Q_L = \frac{f_0}{\Delta f}. \tag{2.34}$$

Similarly, the Q factor can be calculated through the change of phase for a series resonator as

$$Q = \frac{\omega_0}{2} \frac{\partial \phi(Z_s)}{\partial \omega}\bigg|_{\omega=\omega_0}. \tag{2.35}$$

The complex characteristic impedance of a resonator coupled to a microstrip line can be found using the method proposed by [36]. If we assume that we have a two-port fixture free from electrical imperfections, we can find the resonator impedance as

$$Z = 2Z_0 \left[\frac{S_{21e}}{S_{21o}} - 1\right], \tag{2.36}$$

where Z_0 is the characteristic impedance of the transmission line, S_{21e} is the average of the measured S_{12} and S_{21} scattering parameters for the empty two-port fixture, and S_{21o} is the average of the measured S_{12} and S_{21} scattering parameters with the resonator present.

2.7 Multiline method

The multiline method, presented by Roger B. Marks [37], can be used to find the propagation constant from two transmission lines. A transmission line with length l_i connected to a VNA, can be represented by the cascade matrix M_i as

$$M_i = AT^iB, \tag{2.37}$$

where A and B are matrices representing imperfections in the VNA and cable connections [37], [38]. The matrix T^i represents the cascade matrix of a transmission line with length l_i,

$$T^i = (U + \delta^{1i}) L^i \overline{(U + \delta^{2i})}, \tag{2.38}$$

where L^i is the representation of an ideal transmission line

$$L^l = \begin{bmatrix} e^{-\gamma l_i} & 0 \\ 0 & e^{+\gamma l_i} \end{bmatrix}. \tag{2.39}$$

The matrices δ^{1i} and δ^{2i} represent imperfections in the transmission line [37]. For the rest of this analysis, we will assume a perfect transmission line and let $T^i \equiv L^i$. We can write the cascade matrix M^i in terms of measured S parameters,

$$M^i = \frac{1}{S_{21i}} \begin{bmatrix} (S_{12i}, S_{21i} - S_{11i}, S_{22i}) & S_{11i} \\ -S_{22i} & 1 \end{bmatrix} \text{ [38]}. \tag{2.40}$$

Given two transmission lines with lengths l_i and l_j and corresponding cascade matrices M^i, M^j, we can define a new matrix M^{ij} as

$$M^{ij} \equiv M^j (M^i)^{-1}. \tag{2.41}$$

For two ideal transmission lines, we can follow the same procedure and define T^{ij} as

$$\begin{aligned} T^{ij} &\equiv T^j (T^i)^{-1} \\ &= \begin{bmatrix} e^{-\gamma(l_j - l_i)} & 0 \\ 0 & e^{+\gamma(l_j - l_i)} \end{bmatrix}. \end{aligned} \tag{2.42}$$

These matrices are related to each other by

$$M^{ij} X = X T^{ij}, \tag{2.43}$$

assuming that the imperfections represented by the matrices A and B are the same for both transmission lines and the only difference is the line length. We thus have an eigenvalue problem, where the eigenvalues λ_{ij_1} and λ_{ij_2} give us information about the propagation constant γ. Solving the eigenvalue equation gives an expression for the propagation constant as

$$\gamma = \frac{\ln(\lambda_{ij})}{l_i - l_j}. \tag{2.44}$$

For a broadband measurement, we can solve for each frequency in order to find

$$\gamma(\omega) = \alpha(\omega) + j\beta(\omega). \tag{2.45}$$

From γ we can find the dielectric loss tangent and relative permittivity.

If measurements were performed on a microstrip line, we would not only have dielectric losses α_d, but also conductor losses α_c dependent on the surface resistivity R_s, characteristic impedance Z_0, and line width W,

$$\alpha_c = \frac{R_s}{Z_0 W} \text{ [21].} \tag{2.46}$$

The surface resistivity varies depending on the conductor, but can be calculated through

$$R_s = \sqrt{\frac{\omega\mu_0}{2\sigma}}. \tag{2.47}$$

The conductor loss does not take surface roughness effects into account, which can be modelled by a correction factor

$$C_r = 1 + \frac{2}{\pi}\arctan\left(1.4\left(\frac{\Delta}{\delta_s}\right)^2\right), \tag{2.48}$$

where $\delta_s = \sqrt{\frac{2}{\omega\mu\sigma}}$ is the skin depth and Δ is the RMS surface roughness [39]. The conductor losses can then be written as

$$\alpha_c^{\text{rough}} = C_r\alpha_c. \tag{2.49}$$

For a microstrip line, the characteristic impedance is in turn dependent on the ratio between the line width and substrate thickness d

$$Z_0 = \begin{cases} \frac{120\pi}{\sqrt{\varepsilon_e}\left[\frac{W}{d}+1.393+0.667\ln\left(\frac{W}{d}+1.444\right)\right]} & \frac{W}{d} \geq 1 \\ \frac{60}{\sqrt{\varepsilon_e}}\ln\left(\frac{8d}{W}+\frac{W}{4d}\right) & \frac{W}{d} \leq 1, \end{cases} \tag{2.50}$$

where ε_e is the effective dielectric constant given by

$$\varepsilon_e = \frac{\varepsilon_r+1}{2} + \frac{\varepsilon_r-1}{2}\frac{1}{\sqrt{1+12\frac{d}{W}}} \text{ [21].} \tag{2.51}$$

The dielectric loss α_d can then be found assuming $\alpha = \alpha_c^{\text{rough}} + \alpha_d$, Equation 2.45, and the definition of dielectric loss for a microstrip line given by [21] as

$$\begin{aligned} \alpha_d &= \text{Re}(\gamma) - \alpha_c^{\text{rough}} \\ &= \frac{k_0\varepsilon_r\left(\varepsilon_e-1\right)\tan\delta}{2\sqrt{\varepsilon_e}\left(\varepsilon_r-1\right)}. \end{aligned} \tag{2.52}$$

The imaginary part of the propagation constant for a microstrip line is given by

$$\beta = \text{Im}(\gamma) = k_0\sqrt{\varepsilon_e} \tag{2.53}$$

which together with Equation 2.51 can be used to extract the relative permittivity ε_r. From this, the loss tangent can be found using Equation 2.52. Errors in γ for this method arise when there are mismatches in impedance as well as connector discrepancies [40], [41].

3

Ceramic Additive Manufacturing

To manufacture ceramic components, ceramic powder has to be formed into the desired shape by molding, pressing, casting, machining, or other methods [42]. However, these techniques can be costly when fewer batches of complex geometries need to be produced. To reduce these limitations, alternative manufacturing processes are being explored. One of them is additive manufacturing, also called 3D printing. Additive manufacturing is the process of building physical three-dimensional structures from computer models. To create ceramic additively manufactured parts, there are several methods available. One approach, and the method used for this thesis, is Lithography-Based Ceramic Manufacturing (LCM).

Fabrication of the 3D printed components was performed at Chalmers Centre for Additive Manufacture, CAM2. This was done using LCM with the Lithoz CeraFab Multi 2M30, a 3D printer that has the capacity to perform multi-material printing [43]. The LCM process uses a layer-by-layer technique in order to build components from a slurry [44], [45]. The slurry consists of a mixture between the ceramic material, photocurable binder, plasticizers and dispersants [44]. The manufacturing process is as follows:

1. A slurry is deposited on a transparent vat and spread out using a blade to the desired layer thickness.
2. The moveable build platform is lowered and dipped into the slurry.
3. The slurry is selectively exposed to visible blue light from beneath the vat with the help of a digital micromirror device (DMD), curing the photopolymer only in the exposed area. The DMD divides the available printing area into a number of pixels that are either on or off.
4. The building platform lifts the cured part out of the vat.
5. The slurry is spread out again on the vat and the process repeats.

After the component has been produced, we have what is called a green body. In order to get the finished part with the desired properties, we have to debind and sinter the green part. These steps are performed for conventional ceramic manufacturing processes as well [44].

After printing, the parts are cleaned with Lithasol 20 and air-brushed to remove any uncured slurry. Afterwards they are left to air-dry for a few hours and are stored in a desiccator before debinding. Each sample is individually debinded in a thermal analyser (NETZSCH STA 449 F1 Jupiter), following Lithoz standard

cycle for components with wall thickness between 1−3 mm. This is done in order to remove all the binding materials. The temperature cycle is shown in Figure 3.1.

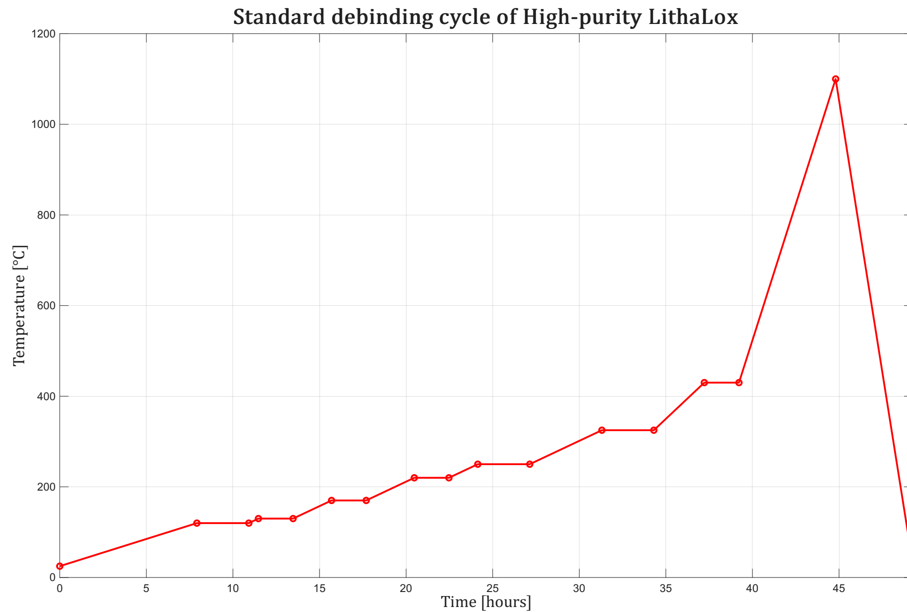

Figure 3.1: Temperature cycle for debinding the green body after fabrication.

After the binding material is removed, we have a porous body. Sintering is performed in order to densify the body and transform it to a continuous structure dominated by grains and grain boundaries. This is done by heating the component to high temperatures. The temperature cycle for the sintering process is presented in Figure 3.2.

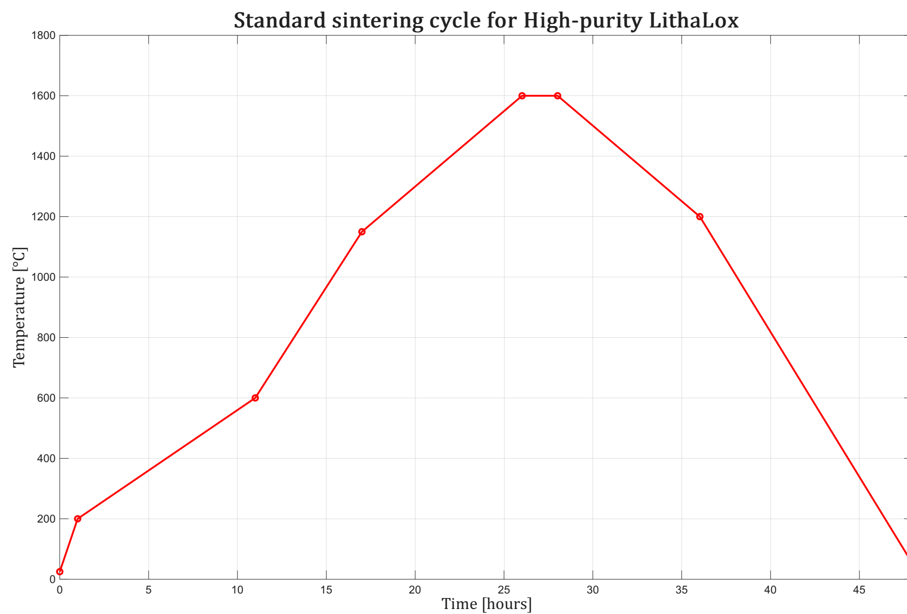

Figure 3.2: Temperature for sintering the porous alumina component.

Because of the densification after debinding and sintering, shrinkage rates are specified before printing in order to accommodate for the change in size. In the XY-direction the shrinkage rate was 24.5%, and 27.5% in the Z direction.

The final component can be erroneous as a consequence of the fabrication process. During the upward pull of the platform after the slurry has been cured, tensile stress may develop in the sample which in turn could lead to layer defects [42]. There is also the possibility of uneven material distribution. If a material is difficult to cure and the material has insufficient stability against settling, the particles can accumulate at the bottom of the layer. By increasing the energy of light when curing, this effect can be mitigated. However, the power increase can cause high polymerisation rates and heat release which in turn could deform the cured part. There can also be a polymerisation gradient within individual layers, which can cause cracks during debinding [46].

The material used for the ceramic components is High-Purity LithaLox from Lithoz, which contains high-purity aluminium oxide powder [47]. The sintered material properties are presented in Table 3.1.

Table 3.1: Material parameters of sintered high-purity LithaLox from Lithoz, containing high-purity aluminium oxide [47].

Sintered Ceramic	
Theoretical density	3.985 g cm^{-3}
Relative density	99.4 %
Surface roughness, R_a	0.4 µm
Relative permittivity (@ 7.5 GHz)	9.9
Dielectric loss tangent (@ 7.5 GHz)	9×10^{-5}
Maximum working temperature	1650 °C

3.1 Hot Isostatic Pressing

As stated in Table 3.1, the relative density of sintered alumina is 99.4 %. In order to achieve full density of the ceramic component, additional post-processing may be necessary. One way to do this is by Hot Isostatic Pressing (HIP), a high-temperature high-pressure process that can densify components to near-theoretical density [48]. This process can mitigate internal defects such as porosity, voids, and microcracks. Some of the samples produced at Chalmers were sent to Quintus for this HIP process. The pressure and temperature cycle is shown in Figure 3.3.

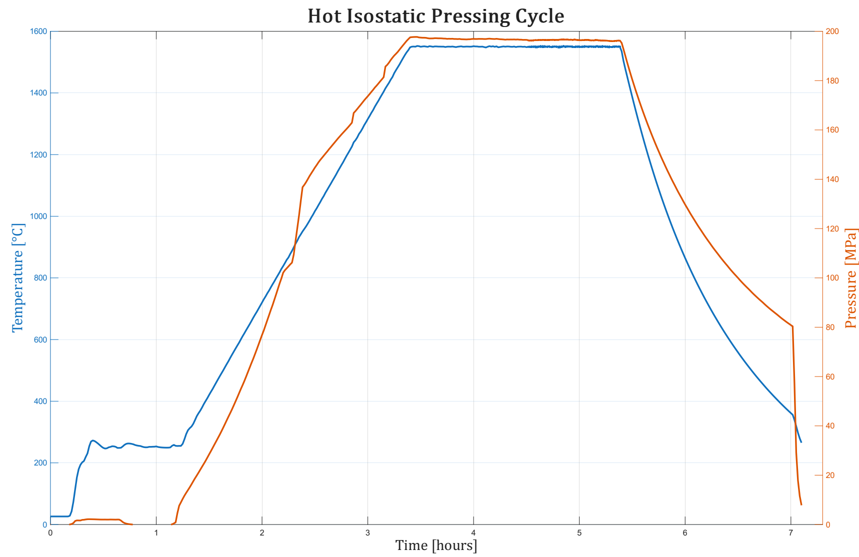

Figure 3.3: Temperature and pressure cycle for the HIP process at Quintus.

The densities after sintering and HIP are presented in Table 3.2 for three cubes used for the measurement method presented in Section 4.1. The measured dimensions are presented in Table 4.1.

Table 3.2: Measured density and relative density of samples after sintering, before and after HIP. The density measurement was performed using the Archimedes principle and compared to the theoretical density in Table 3.1

Sample	**Sintered**		**HIPed**	
	Density ($\mathrm{g\,cm^{-3}}$)	**Relative density** (%)	**Density** ($\mathrm{g\,cm^{-3}}$)	**Relative density** (%)
Cube 1	3.8668	96.91	3.9278	98.44
Cube 2	3.9091	97.97	3.9170	98.17
Cube 3	3.9416	98.79	3.9486	98.96

An image of the final HIPed and sintered cubes is presented in Figure 3.4. Note that the image is taken after application of copper tape, which is needed in order to measure them as parallel plate capacitors.

Figure 3.4: Sintered and HIPed additively manufactured cubes, with densities presented in Table 3.2. Note that copper tape is attached to them in this figure, which was done after the density measurements. The dimensions are given in Table 4.1.

4
Method

In this section, the three proposed methods for measuring the dielectric properties of additively manufactured materials are presented.

4.1 Parallel plate capacitor

The impedance of a parallel plate capacitor can be measured in order to extract the relative permittivity and loss tangent.

4.1.1 Measurement setup

One-port S-parameter measurements were performed using Keysight Vector Network Analyser E5061B connected to a Keysight 16201A 7 mm Terminal Adapter with a Keysight 16192A Parallel Electrode SMD Test Fixture on top. The measurement setup is presented in Figure 4.1a.

(a) Measurement setup for one-port S-parameter characterisation of a parallel plate capacitor.

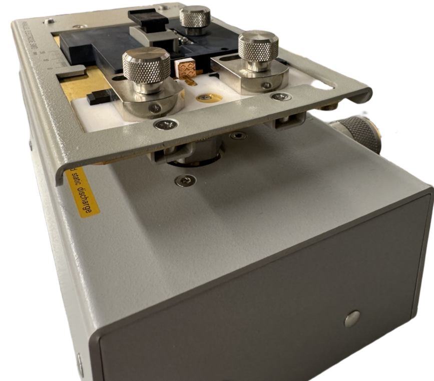

(b) Close-up of the Keysight 16192A test fixture with the sintered and HIPed 3D-printed cube in position.

Figure 4.1: Measurement setup used for one-port S-parameter characterization of the parallel plate capacitor. (a) Overview of the setup consisting of a Keysight E5061B VNA, a Keysight 16201A 7 mm terminal adapter, and a Keysight 16192A parallel electrode SMD test fixture. (b) Close-up of the test fixture with the sample mounted.

The measurements were performed on 3D printed cubes of various sizes, with copper tape applied on the top and bottom in order to form a parallel plate capacitor. Short-Open-Load calibration was performed with Maury Microwave 2650CK10 calibration kit at the terminal adapter. A close-up of the cube on the SMD test fixture can be seen in Figure 4.1b.

In order to analyse the impact of the fabrication process, measurements were made on green body cubes, sintered cubes, as well as cubes that had undergone both sintering and HIP. The sizes of the cubes are presented in Table 4.1.

Table 4.1: Dimensions of 3D-printed cubes before and after processing. An image of the sintered and HIPed cubes are given in Figure 3.4 and the green body cubes in Figure 4.2.

Processing state	Measurement	Cube 1	Cube 2	Cube 3	Cube 4
Green body	Area (mm^2)	5.618 × 5.626	5.637 × 5.598	5.534 × 5.536	5.567 × 5.560
	Height (mm)	1.171	1.806	2.423	3.044
Sintered	Area (mm^2)	4.614 × 4.598	4.487 × 4.516	4.524 × 4.485	–
	Height (mm)	0.982	1.430	1.937	–
Sintered + HIP	Area (mm^2)	4.575 × 4.596	4.536 × 4.508	4.488 × 4.493	–
	Height (mm)	0.975	1.418	1.929	–

An image of the sintered and HIPed cubes is presented in Figure 3.4 and the green body cubes are shown in Figure 4.2 below. Note that copper tape is attached to the 3D printed cubes in these images, which is done after measurements.

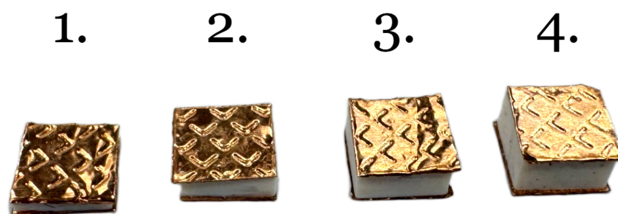

Figure 4.2: Green body additively manufactured cubes, with dimensions presented in Table 4.1. Note that copper tape is attached to them in this figure, which was done after size measurements.

After HIP, the thermal stability of the finished pieces were studied. In order to do this, the measurement setup was modified to be performed inside a ESPEC SH-242 temperature and humidity chamber. The humidity was not modified and the measured temperature values were 25 °C, 30 °C, 40 °C, 50 °C, 60 °C, 70 °C, 80 °C, 90 °C, and 100 °C. A phase-stable coaxial cable was connected between the fixture inside the chamber and the VNA. The S-parameters were saved after the temperature had stabilised. The measurement setup inside the temperature chamber is presented in Figure 4.3.

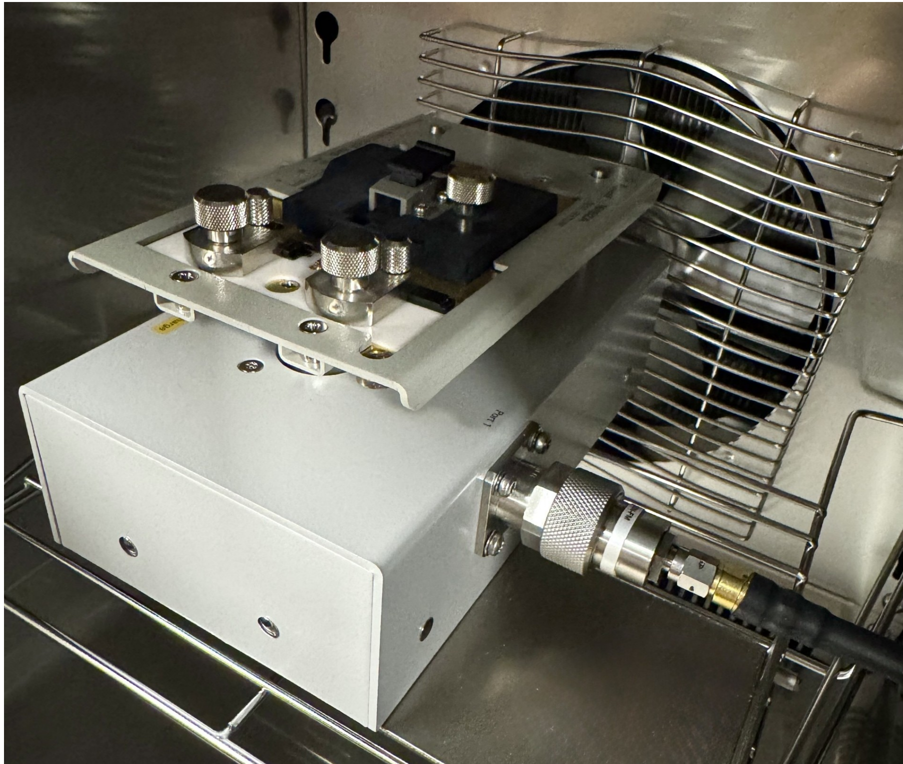

Figure 4.3: Measurement setup inside the ESPEC SH-242 temperature and humidity chamber. A phase-stable coaxial cable connects the test fixture to the VNA.

4.1.2 Extraction of dielectric properties

To extract the dielectric properties, the measured S_{11}-parameters were converted to impedance parameters using `MATLAB`. The impedance values were used in order to see which frequencies belonged to the capacitive region of the capacitor, while the admittance was used to calculate the relative permittivity and loss tangent. The admittance parameters are proportional to C_0, which in turn is proportional to $\frac{A}{h}$. Assuming a constant parasitic conductance and susceptance, we write

$$\begin{aligned} G_{\text{measured}} &= G_{\text{device}} + G_{\text{parasitic}} \\ B_{\text{measured}} &= B_{\text{device}} + B_{\text{parasitic}} \end{aligned} \tag{4.1}$$

where $G_{\text{device}} \propto \frac{A}{h}$, $B_{\text{device}} \propto \frac{A}{h}$. With this, we can use linear regression in order to find the slope between the measure capacitances for the different cubes of varying dimensions. For example, using the conductance the slope would be a function of the device parameter and dimension $k_G = \frac{G_{\text{device}}}{A/h}$. The implementation of this method follows that of Algorithm 1, where `polyfit` is a `MATLAB` function that returns polynomial coefficients using the least-squares method.

Algorithm 1 Extraction of dielectric properties using the parallel plate capacitor method

for each frequency in the capacitive region **do**
  for each cube **do**
    Calculate capacitance $C = \frac{\text{Im}(Y_{11})}{\omega}$
    Calculate conductance $G = \text{Re}(Y_{11})$
    Calculate geometry factor $x = \frac{A}{h}$
  end for
  Calculate k_C from the slope of the linear regression using `polyfit`(x, C)
  Calculate k_G from the slope of the linear regression using `polyfit`(x, G)
  Calculate $\varepsilon_r = k_C/\varepsilon_0$
  Calculate $\tan\delta = k_G/\omega k_C$
end for
plot ε_r and $\tan\delta$

When studying the temperature stability, Algorithm 1 is repeated for each temperature.

4.2 Resonator coupled to microstrip line

In order to analyse the dielectric properties at higher frequencies, we investigate a dielectric resonator coupled to a microstrip line. Both experimental measurements as well as simulations are performed in order to evaluate the 3D printed resonator.

4.2.1 Measurement setup

The measurements were performed with a Keysight N5247B PNA-X Network Analyser, two 2.4 mm coaxial cables, male to female 2.4 to 2.92 mm coaxial adapter, and a microstrip line designed to be 50 Ω at 11 GHz. The measurement setup is presented in Figure 4.4.

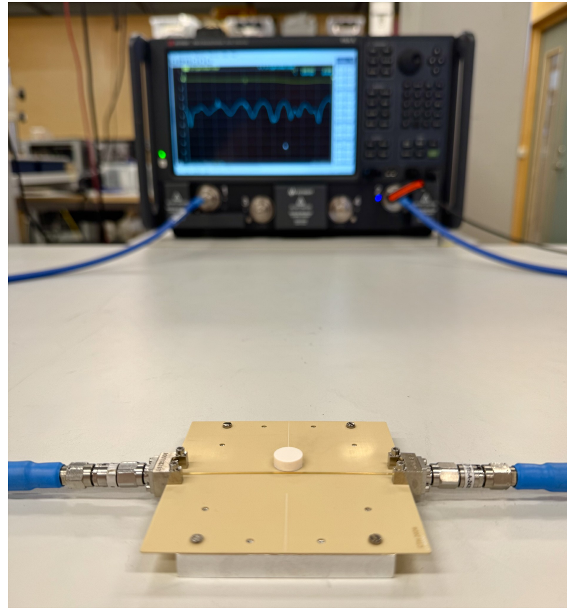

Figure 4.4: Setup for measuring a dielectric resonator coupled to a microstrip line. The measurements were performed with a Keysight N5247B PNA-X Network Analyser, two 2.4 mm coaxial cables, male to female 2.4 to 2.92 mm coaxial adapter, and a microstrip line designed to be 50 Ω at 11 GHz

In order to get accurate results, a TRL kit was designed on the same substrate as the microstrip line using the same connectors. Both PCBs were fabricated at Eurocircuit with the I-Tera MT40 substrate, which has a relative permittivity of $\varepsilon_r = 3.38$ and loss tangent of $\tan\delta = 0.0028$ measured at 10 GHz. The calibration kit uses one line standard, where the line is 90° at 11 GHz with a frequency span of around 3 GHz to 19 GHz. The connectors are 2.92 Southwest end launch connectors. An image of the calibration kit is presented in Figure 4.5.

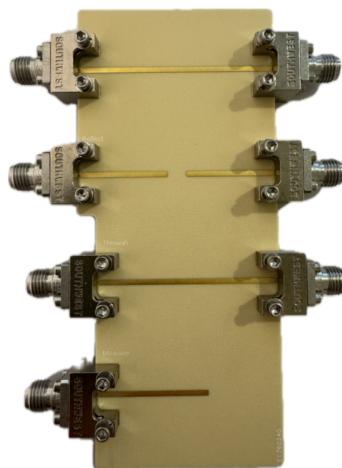

Figure 4.5: TRL calibration kit with one line standard, designed to be 90° at 11 GHz with a frequency span of around 3 GHz to 19 GHz. The connectors are 2.92 Southwest SMA end launch connectors.

4.2.2 Simulation setup

The simulations were performed using the electromagnetic field simulator program Advanced Design System (ADS). Both 3D simulations using the finite element method (FEM) as well as schematic simulations were performed. For the FEM simulations, a substrate stack has to be defined. This is done in layers, were we have the 0.5 mm thick MT40 substrate as a base. Under, we define a ground plane and on top a conductor. The resonator is defined as a dielectric medium, with characteristics first defined from Table 3.1. The substrate model is shown in Figure 4.6.

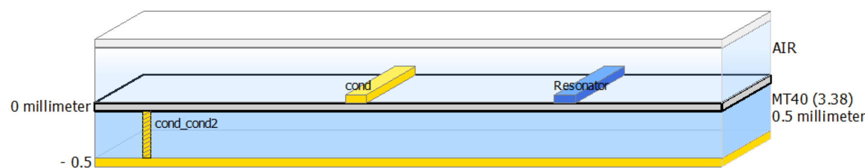

Figure 4.6: Substrate stackup in ADS used in the three-dimensional FEM simulations. The bottom layer is defined as the ground plane, the conductor copper, and the resonator a dielectric medium according to specifics. The MT40 substrate is defined from Eurocircuit datasheet.

To model the resonator coupled to the microstrip line, the resonator height is defined in the substrate and then drawn in ADS. The microstrip line width is designed to be 50 Ω at 11 GHz, and the line length is 40 mm so that the reference plane is the same for the simulations and the measurements after calibration. The three-dimensional model is shown in Figure 4.7. The FEM simulations were performed with standard settings, except for the delta error which was set to 0.01. The ports were of TML type.

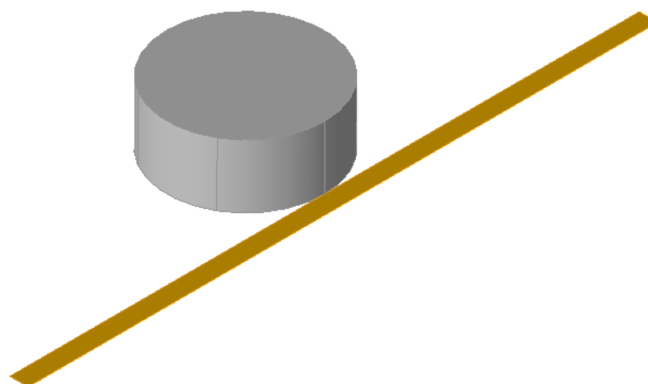

Figure 4.7: Three-dimensional model of the measurement setup in ADS used for FEM simulations. In this example the radius of the resonator is 5 mm and the height 4 mm. The width of the microstrip line is 1.15 mm and the length 40 mm.

For simulations using the schematic tool in ADS, a predefined dielectric resonator

model is used. The coupling factor, relative permittivity, quality factor, and dimensions of the resonator as well as microstrip parameters are inputted. The microstrips were defined on a substrate model of the I-Tera MT40 substrate following the same dimensions as in Figure 4.7 and terminated with $50\,\Omega$ ports.

4.2.3 Extraction of dielectric properties

From the measured and simulated S-parameters, there are several ways to extract the dielectric properties. Using ADS, one can tune ε_r and $\tan\delta$ until the measured and simulations match. Another way is the three-point method, where the resonant frequency and 3 dB bandwidth points are utilised. By finding the resonant frequency f_0, we can calculate the coupling coefficient and loaded quality factor from Equations 2.32 and 2.34. Inserting the result in Equation 2.33, we find the unloaded quality factor of the resonator which is inversely related to the loss tangent. This is implemented in `MATLAB` according to Algorithm 2.

Algorithm 2 Extraction of unloaded Q-factor from the resonant frequency and 3 dB bandwidth points.

$f_0 = f(\min(S_{21,dB}))$
$f_1 = f(\min(S_{21,dB}) - 3\text{dB})$
$f_2 = f(\min(S_{21,dB}) + 3\text{dB})$
$\beta = \frac{S_{11}(f_0)}{S_{21}(f_0)}$
$Q_L = \frac{f_0}{f_2 - f_1}$
$Q_0 = Q_L(1+\beta)$

In order to compare our results, we can use another method to calculate the quality factor. Assuming that we have no electrical imperfections in our measurement setup after calibration, we can use Equation 2.36 to calculate the characteristic impedance of the resonator. From this, we can use Equation 2.35 in order to find the quality factor of the resonator. This is implemented in `MATLAB` according to Algorithm 3.

Algorithm 3 Extraction of Q-factor from the de-embedded resonator impedance.

$S_{21e} = \frac{S_{21e}^{\text{meas}} + S_{12e}^{\text{meas}}}{2}$
$S_{21o} = \frac{S_{21o}^{\text{meas}} + S_{12o}^{\text{meas}}}{2}$
$Z = 2Z_0\left[\frac{S_{21e}}{S_{21o}} - 1\right]$
$\omega_0 = 2\pi f_0$
$Q_0 = \frac{\omega_0}{2}\frac{\partial\phi(Z)}{\partial\omega}\Big|_{\omega=\omega_0}$

These methods do not give us information about the relative permittivity. In order to do that, we can try to find the approximate solution using the equations presented in Section 2.2. For each numerical approximation, we loop through a list of relative permittivities and store the calculated resonant frequency. The implementation of

Equation 2.16 in `MATLAB` is presented in Algorithm 4. This method does not take fringing fields into account and is valid when we have ground planes close to the top and bottom of the resonator.

Algorithm 4 Resonant frequency extraction using Pozar transcendental equation

for each permittivity guess ε_r **do**
  Solve transcendental equation using nonlinear root finding:
    $k_0 \leftarrow \texttt{fsolve}\Big(F(k_0, \varepsilon_r, r, L) = 0\Big)$
  Compute angular resonant frequency:
    $\omega_0 = c\,k_0$
  Compute resonant frequency:
    $f_0 = \omega_0/(2\pi)$
end for
Store f_0 versus ε_r

If the resonator is placed close on top of a ground plane, but far from the top ground plane, its resonant frequency can be approximated using the method proposed by Itoh and Rudokas [27]. The coupled eigenvalue Equation 2.17 is implemented using Algorithm 5.

Algorithm 5 Resonant frequency extraction using Itoh–Rudokas full-wave model

for each permittivity guess ε_{r1} **do**
  Initialize unknown vector:
    $(h, k_0) \leftarrow \texttt{initial guess}$
  Solve coupled nonlinear system:
    $(h, k_0) \leftarrow \texttt{fsolve}(F(h, k_0; \varepsilon_{r1}, \varepsilon_{r2}, r, L, t) = 0)$
  Extract propagation constants:
    $\beta = \sqrt{\varepsilon_{r1} k_0^2 - h^2}$
    $p = \sqrt{\beta^2 - k_0^2}$
    $\gamma = \sqrt{h^2 - k_0^2}$
    $\xi = \sqrt{h^2 - \varepsilon_{r2} k_0^2}$
  Compute resonant frequency:
    $f = \frac{c\,k_0}{2\pi}$
end for
Store f versus ε_{r1}

To instead approximate the resonant frequency when the dielectric resonator is placed in free space, we can use the variational method presented by Konishi *et al.* [26], using Equation 2.18. This is implemented using Algorithm 6.

Algorithm 6 Resonant frequency correction using Konishi perturbation

for each permittivity guess ε_r **do**
  Solve baseline transcendental equation:
    $k_0 \leftarrow \texttt{fsolve}(F(k_0, \varepsilon_r, r, L) = 0)$
  Compute uncorrected angular frequency:
    $\omega_0 = c\,k_0$
  Evaluate field parameters:
    $x_0 = k_0 r, \quad \xi = d/(2r)$
    $\alpha = \sqrt{k_c^2 - k_0^2}, \quad \beta = \sqrt{\varepsilon_r k_0^2 - k_c^2}$
  Compute correction factor:
    $\Delta = \texttt{KonishiCorrection}(k_0, r, L, \varepsilon_r, \alpha, \beta)$
  Apply frequency correction:
    $\omega_{\text{corr}} = \omega_0(1 + \Delta)$
end for
Convert to frequency: $f_{\text{corr}} = \omega_{\text{corr}}/(2\pi)$

4.3 Multiline method

The multiline method can be used in order to extract the propagation constant using S-parameter measurements from two transmission lines of different lengths.

4.3.1 Measurement setup

The measurement setup follows that of the previous section – Keysight N5247B PNA-X Network Analyzer, two 2.4 mm coaxial cables, male to female 2.4 to 2.92 mm coaxial adapter – but instead of measuring on the microstrip line we measure the Through and Line standard of the TRL kit presented in Figure 4.5. The length difference between them is 4.14 mm. The VNA is calibrated using an electronic calibration kit, Keysight N4691B Ecal 3.5mm, where the reference plane is after the 2.4 mm coaxial cable, before the adapter.

4.3.2 Simulation setup

In order to verify and compare the results, a simple schematic microstrip simulation was set up in ADS. The width of the microstrip line is 1.15 mm, the Through length is 38.3 mm, and the Line length is 42.44 mm.

4.3.3 Extraction of dielectric properties

Following the theory from Section 2.7 we can calculate the relative permittivity and loss tangent at each measured frequency according to Algorithm 7. The measured S-parameters are compared to those simulated using ADS schematic. For the conductor loss, we assume no surface roughness. This gives us an upper bound of the loss tangent.

Algorithm 7 Extraction of complex permittivity from two microstrip lines of different lengths

for each dataset (measured, schematic) **do**
  Import S-parameters of the short and long transmission lines
  for each frequency **do**
    Convert S-parameters to transmission matrices
      $\mathbf{M}_{\text{short}}$
      $\mathbf{M}_{\text{long}}$
    Form matrix ratio
      $\mathbf{M}_{ij} = \mathbf{M}_{\text{long}}\mathbf{M}_{\text{short}}^{-1}$
    Compute eigenvalues
      $\lambda_1, \lambda_2 = \text{eig}(\mathbf{M}_{ij})$
    Select propagating eigenvalue λ
    Calculate propagation constant
      $\gamma = \dfrac{\ln(\lambda)}{L_{\text{short}} - L_{\text{long}}}$
    Extract attenuation and phase constants
      $\alpha = \text{Re}(\gamma)$
      $\beta = \text{Im}(\gamma)$
    Calculate effective permittivity
      $\varepsilon_{\text{eff}} = \left(\dfrac{\beta}{k_0}\right)^2$
    Calculate dielectric constant using the microstrip model
      $\varepsilon_r = \dfrac{2\varepsilon_{\text{eff}} - (1-u)}{1+u}$
    Calculate characteristic impedance Z_0
    Calculate conductor loss
      $\alpha_c = \dfrac{R_s}{Z_0 w}$
    Calculate dielectric loss
      $\alpha_d = \alpha - \alpha_c$
    Calculate loss tangent
      $\tan\delta = \dfrac{2\alpha_d\sqrt{\varepsilon_{\text{eff}}}(\varepsilon_r - 1)}{k_0\varepsilon_r(\varepsilon_{\text{eff}} - 1)}$
  end for
end for
Plot ε_r and $\tan\delta$ versus frequency

5

Results

Using the methods presented in Section 4, the results for the different setups are presented and discussed in this section.

5.1 Parallel plate capacitor measurements

Green body, sintered, and HIPed samples were measured in order to compare dielectric properties across fabrication stages. The relative permittivity increased after each processing step, as shown in Figure 5.1.

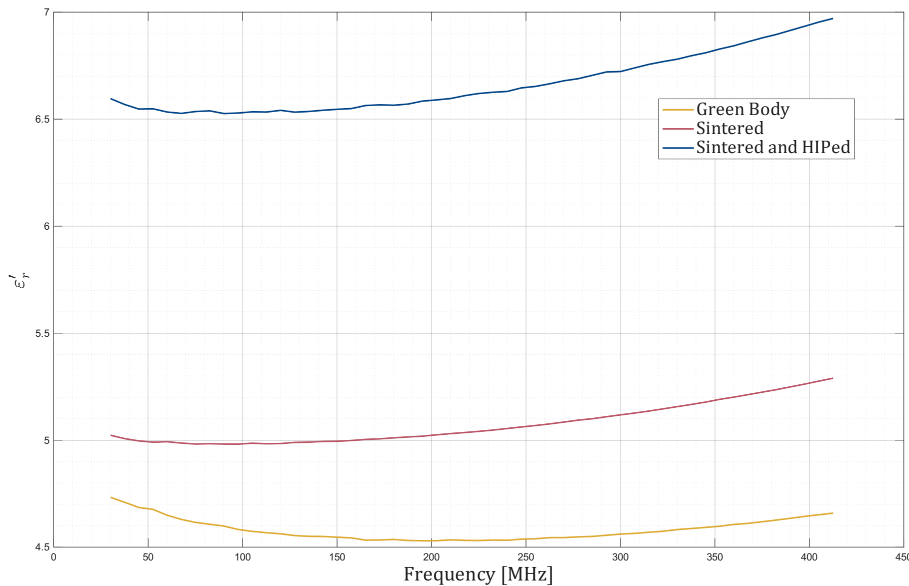

Figure 5.1: Relative permittivity of the additively manufactured cubes as a function of frequency. There is a clear increase in permittivity after HIP.

The loss tangent decreased with each fabrication stage instead, which can be seen in Figure 5.2.

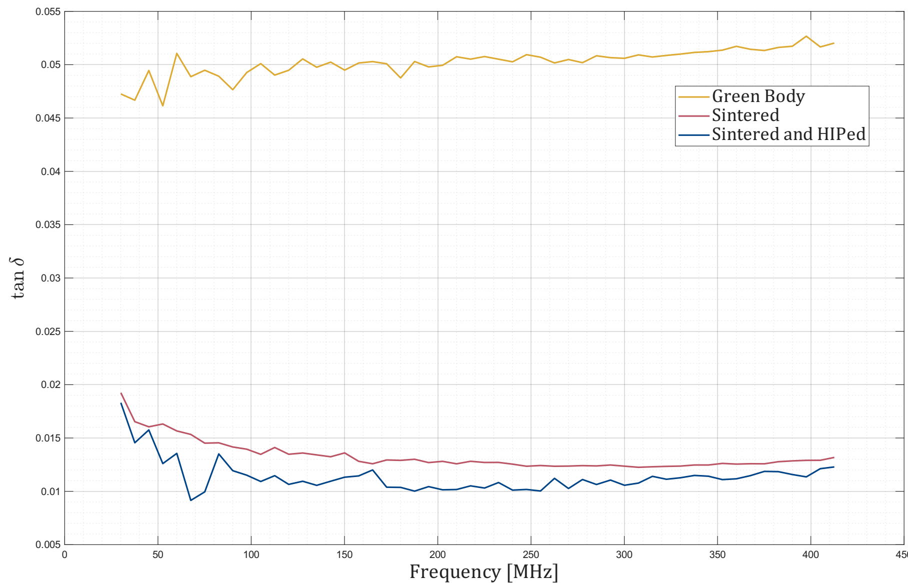

Figure 5.2: Loss tangent of the additively manufactured cubes as a function of frequency, after linear regression. The loss tangent decreases after sintering.

The average relative permittivity and loss tangent over the frequency span are presented in Table 5.1, and compared to the material properties as specified by Lithoz after sintering (at 7.5 GHz).

Table 5.1: Average relative density and dielectric properties of the printed alumina samples at different processing stages.

Sample	**Relative density (%)**	ε_r	$\tan\delta$
Green body	–	4.6	5.0×10^{-2}
Sintered	97.9	5.1	1.3×10^{-2}
Sintered + HIP	98.5	6.7	1.1×10^{-2}
Lithoz specification	99.4	9.9 (@ 7.5 GHz)	9.0×10^{-5} (@ 7.5 GHz)

A 0.6 % increase in density resulted in a 31.4 % increase in relative permittivity and a 15.4 % decrease in loss tangent. These trends are consistent with the findings reported by Penn et al. [29] and Jenkel et al. [30], who observed a strong dependence of dielectric properties on material density. Nevertheless, the measured dielectric properties remain below the values specified by Lithoz. Since the measured densities of the sintered samples also remain below the manufacturer's specified density, the results suggest that further improvements in relative permittivity and reductions in loss tangent may be achievable through additional densification.

For all samples, the measured loss tangent exceeded the value reported by Lithoz. One possible explanation is that the loss tangent is particularly sensitive to measurement uncertainties and model assumptions. For example, some sample dimensions measured after HIP were larger than those measured before HIP, despite the increase

in density. This observation indicates uncertainty in the geometric measurements, which directly affects the calculated dielectric properties. Furthermore, the extraction method assumed constant parasitic contributions and used linear regression to determine the device parameters as a function of the area-to-height ratio of the cubes. This method was proposed due to a variation in dielectric properties dependent on the sample size, as seen in Figure 5.3, which should not be the case if all samples are of the same material.

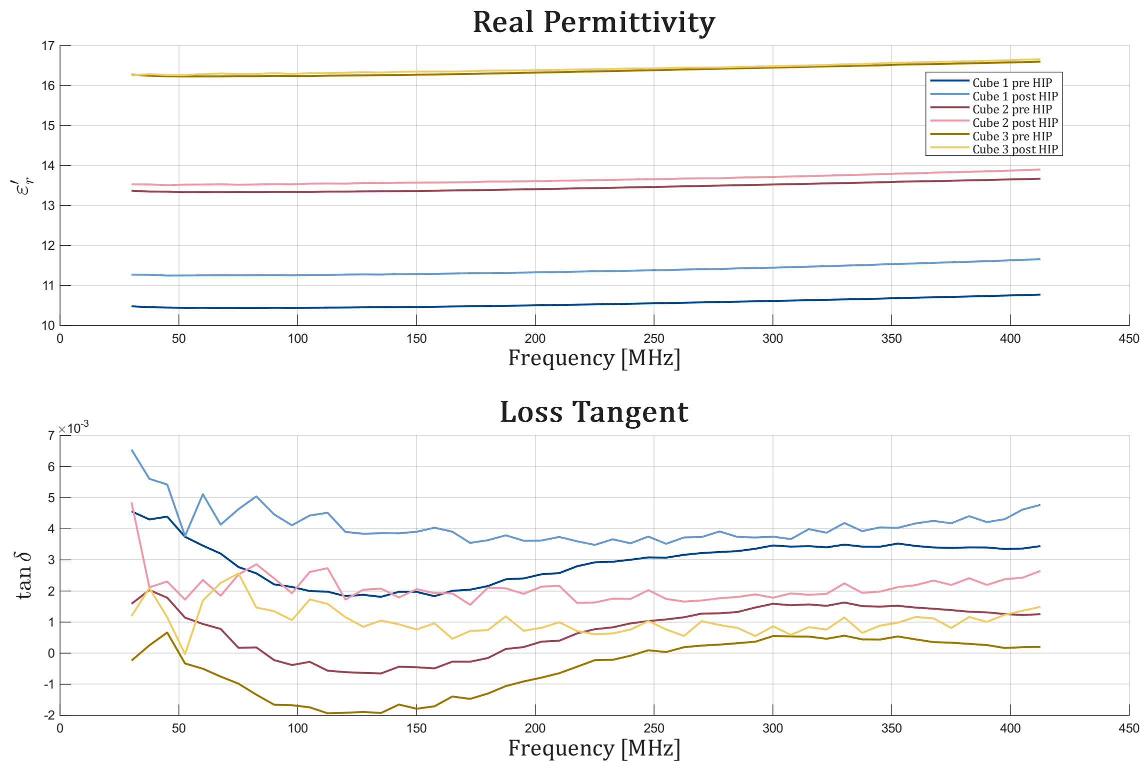

Figure 5.3: The calculated relative permittivity and loss tangent of the additively manufactured cubes before and after HIP, without the use of a linear regression approximation. The permittivity and loss tangent seem to have a size dependence.

As presented in Table 3.2, the cubes have different densities both before and after HIP. This means that there could be slight differences in the dielectric properties between the cubes, which could influence the linear regression results. Despite this, the linear fits shown in Figure 5.4 demonstrate good agreement for all sintered as well as sintered and HIPed samples. The primary exception is the green body measurements, which exhibited larger deviations. This behaviour is likely related to the high porosity of the green bodies, which made the dimensions harder to measure accurately.

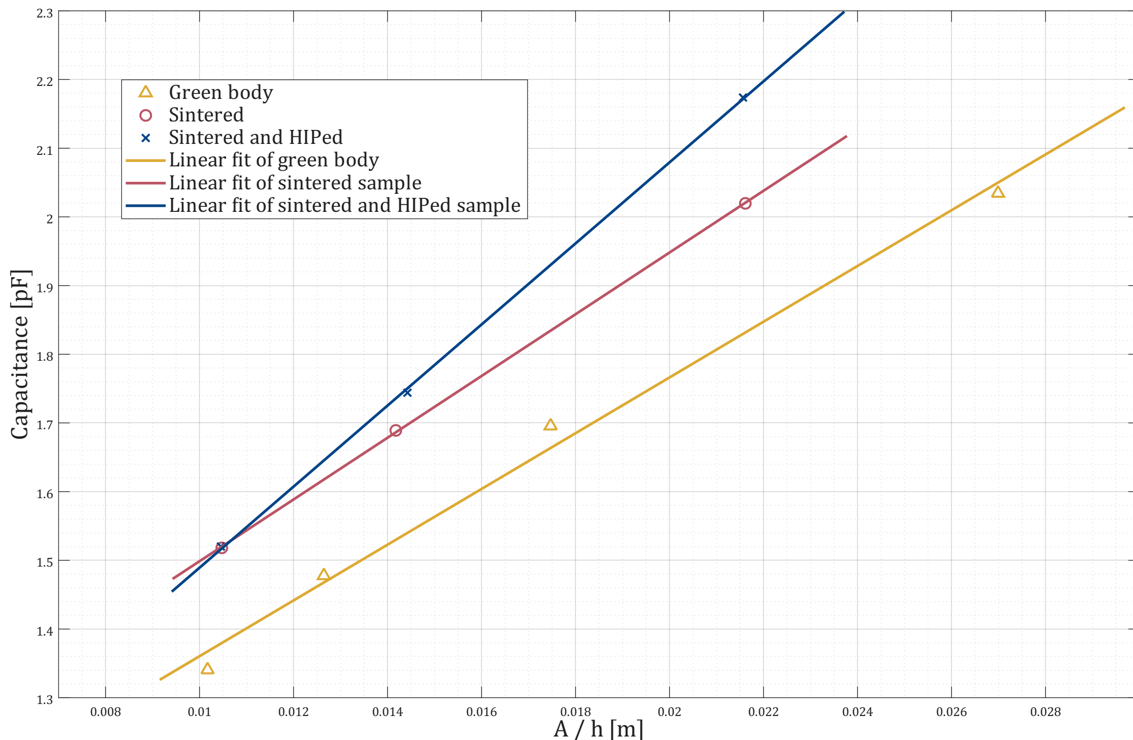

Figure 5.4: Linear regression of capacitance as a function of the area divided by height of the 3D printed cubes. The sintered, and sintered and HIPed cubes have a good linear fit compared to the green body cubes.

Nevertheless, a clear correlation between the relative density and the relative permittivity can be observed. This trend is consistent with previous studies that have reported an increase in permittivity with increasing densification due to the reduction of porosity.

The influence of density on the loss tangent is less straightforward. Penn *et al.* [29] demonstrated that dielectric loss is highly sensitive to porosity, suggesting that the elevated loss tangent measured in the present work may partly be attributed to the lower relative density of the samples compared with the manufacturer's specification. However, the measured HIPed samples reached relative densities of up to 98.5%, compared with the specified value of 99.4%, while the corresponding loss tangent remained approximately two orders of magnitude higher than the specified value. Furthermore, the transition from the sintered to the HIPed state resulted in oa 0.6% increase in relative density and a 15.4% reduction in loss tangent. These observations indicate that porosity alone is unlikely to fully explain the discrepancy. Measurement uncertainty may have contributed to the observed difference. The dielectric properties extracted using the parallel plate capacitor method are sensitive to uncertainties in sample dimensions, electrode contact quality, fixture parasitics, and calibration accuracy. Since the loss tangent is derived from relatively small conductive losses, even small measurement errors can have a significant impact on the extracted values. Consequently, both microstructural differences and measurement uncertainty should be considered.

Further investigation of the microstructure would be interesting in order to establish the mechanisms underlying the observed dielectric behaviour. In particular, microstructural characterisation of the additively manufactured material could be used to assess the influence of grain size and porosity on the dielectric properties. This would enable a direct comparison with the findings of Jenkel et al. [30], who reported significant correlations between dielectric performance, grain size, and porosity.

Measurements were also conducted to investigate the temperature dependence of the dielectric properties. The average relative permittivity varied by less than 2 % between 25 °C and 100 °C. This can be seen in Figure 5.5.

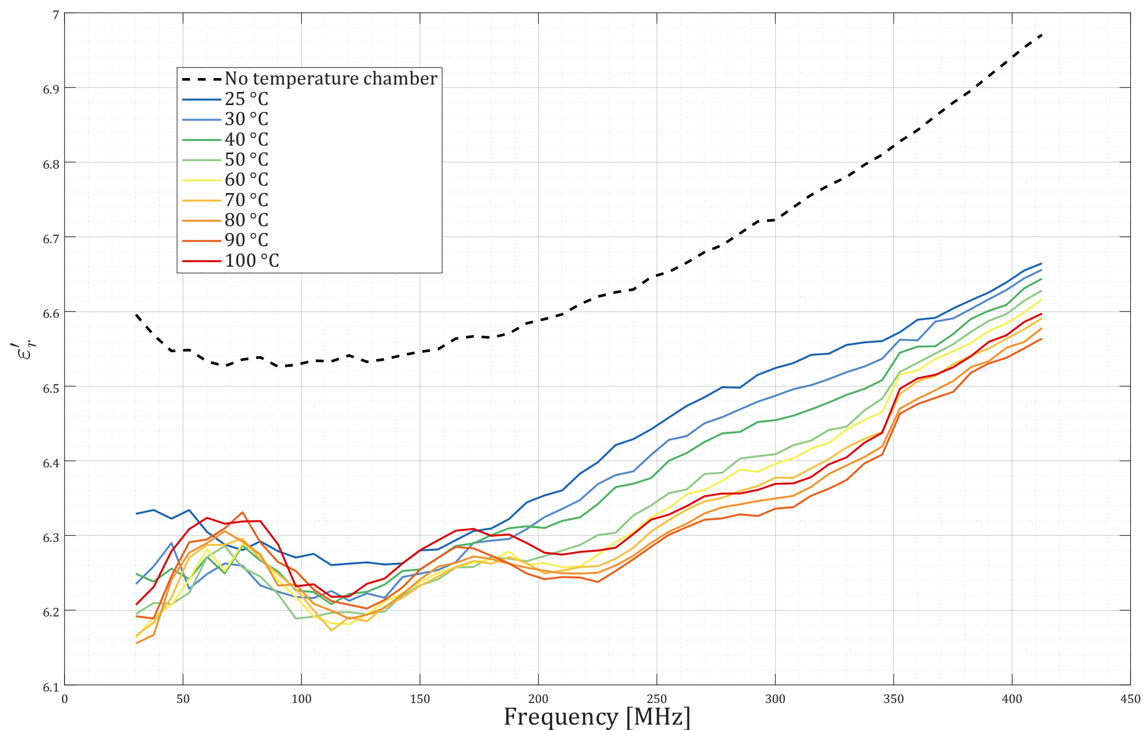

Figure 5.5: Measurements of relative permittivity over temperature for sintered and HIPed cubes, compared with results from measuring outside of the temperature chamber. The discrepancy between outside and inside temperature chamber could be because of interference with the shielded chamber. The average relative permittivity varied by less than 2 % over the temperature span.

As seen in Figure 5.5, there is a discrepancy between the relative permittivity measured inside and outside of the temperature chamber. Since the chamber is a metal box, the difference between measurement results could be due to interference with the shielded chamber.

For the dielectric loss, an increase of approximately 250 % is observed, as illustrated in Figure 5.6. This indicates a strong apparent temperature dependence of the loss tangent over the investigated temperature range. However, part of this variation may also be influenced by measurement conditions and the sensitivity of the loss tangent to parasitic effects.

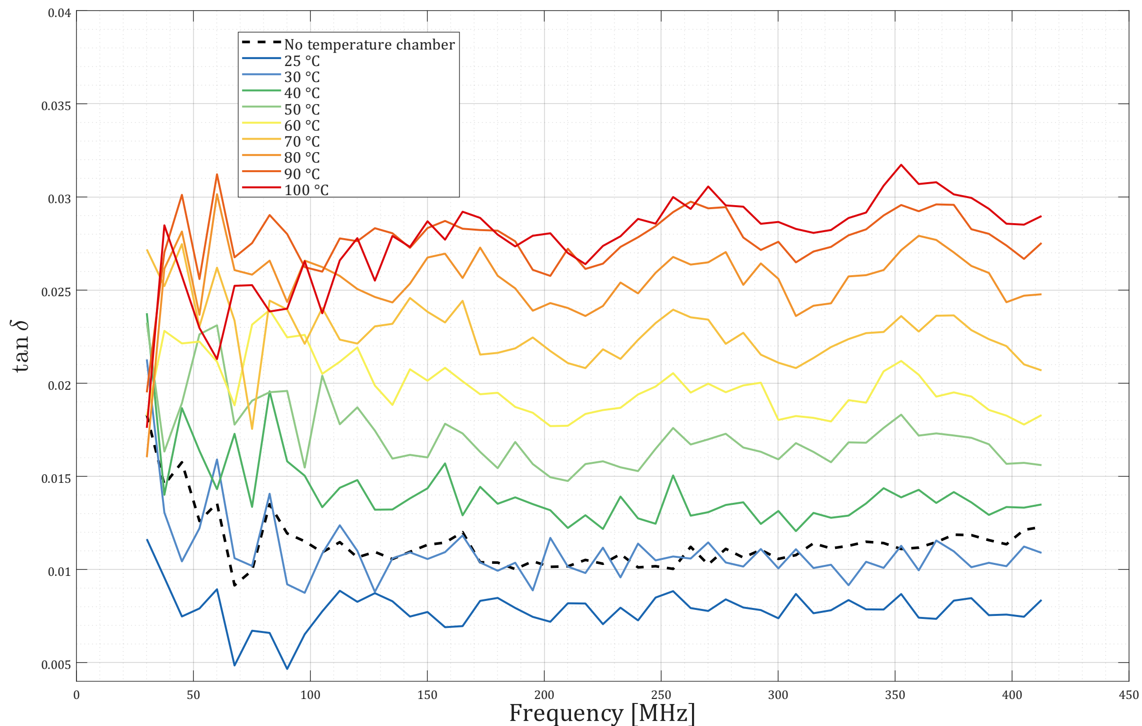

Figure 5.6: Measurements of loss tangent over temperature for sintered and HIPed cubes, compared with results from measuring outside of the temperature chamber. The loss increases with temperature.

It would be of interest to investigate how the temperature dependence of the dielectric properties is influenced by processing parameters such as sintering temperature and relative density. In particular, it would be valuable to determine whether increased densification reduces the temperature sensitivity of the loss tangent. Furthermore, temperature-dependent measurements using the two alternative characterisation methods would provide an independent validation of the observed trends and enable a comparison of the methods' consistency and accuracy.

5.2 Resonator coupled to microstrip line

A green body cylinder was placed beside a microstrip line in order to investigate whether a resonant response could be observed. As presented in Figure 5.7, no distinct resonance response was found within the frequency range. One possible explanation is the high polymer content and porosity of the green body. Figure 5.7 also includes FEM simulation results obtained using ADS. The simulations were performed using the dielectric properties extracted from the parallel plate capacitance measurements of the green body. No resonant response was observed in the simulations, following the measured results. For the green body simulations, full-wave FEM simulations were required, as the schematic-based resonator model available in ADS could only be simulated with $\varepsilon_r \geq 6$. Since the measured relative permittivity of the green body was below this threshold, the schematic model was not applicable.

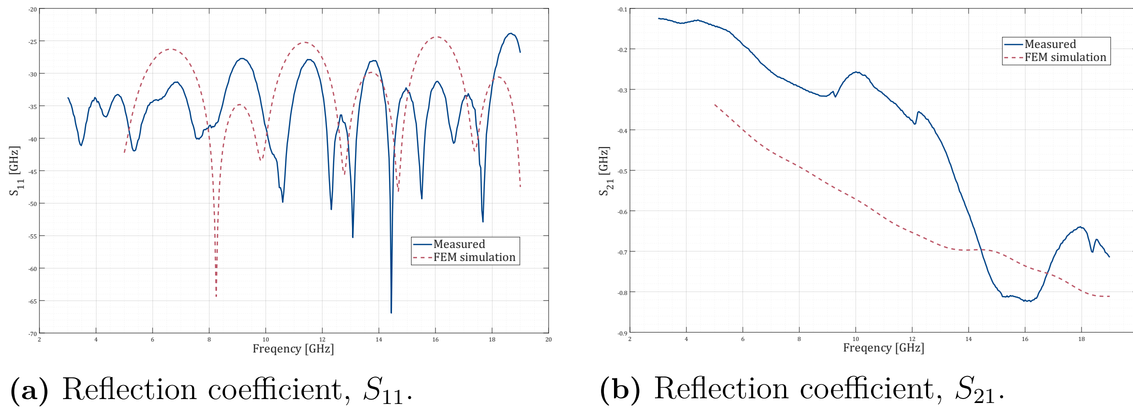

(a) Reflection coefficient, S_{11}.   **(b)** Reflection coefficient, S_{21}.

Figure 5.7: Measured and simulated scattering parameters of a green body dielectric resonator coupled to a microstrip line. (a) Reflection coefficient, S_{11}. (b) Transmission coefficient, S_{21}.

To evaluate the performance of the proposed measurement method, a commercial dielectric resonator (DRT 10.5 GHz) with a specified relative permittivity of $\varepsilon_r = 33$ and a resonant frequency of 10.5 GHz was characterised. When coupled to the microstrip line, the first resonant mode was measured at 11.15 GHz, as shown in Figure 5.8. The discrepancy between the specified and measured resonance frequency could be due to the specified value referring to the intrinsic resonance of the isolated resonator, instead of the loaded resonator.

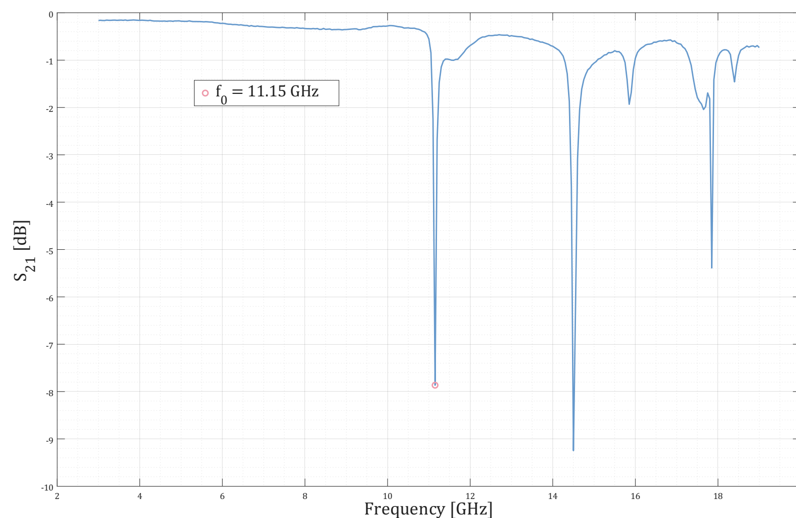

Figure 5.8: Magnitude of the transmission of a microstrip line coupled to a DRT 10.5GHz resonator. The first resonance frequency is 11.15 GHz.

Using Algorithms 2 and 3, the quality factor and coupling coefficient between the microstrip line and the DRT 10.5 GHz resonator were extracted from the measured S-parameters. The unloaded quality factor obtained using the three-point method was used in both the schematic and FEM simulations, while the relative permittivity was adjusted until the simulated resonant frequency matched the measured value. The resulting comparison is shown in Figure 5.9.

In both simulation approaches, a higher relative permittivity than the specified value was required to reproduce the measured resonant frequency. The same resonator geometry was used in both cases, and the schematic dielectric resonator model employed a coupling coefficient of $\beta = 1.49$, calculated from the measured S-parameters.

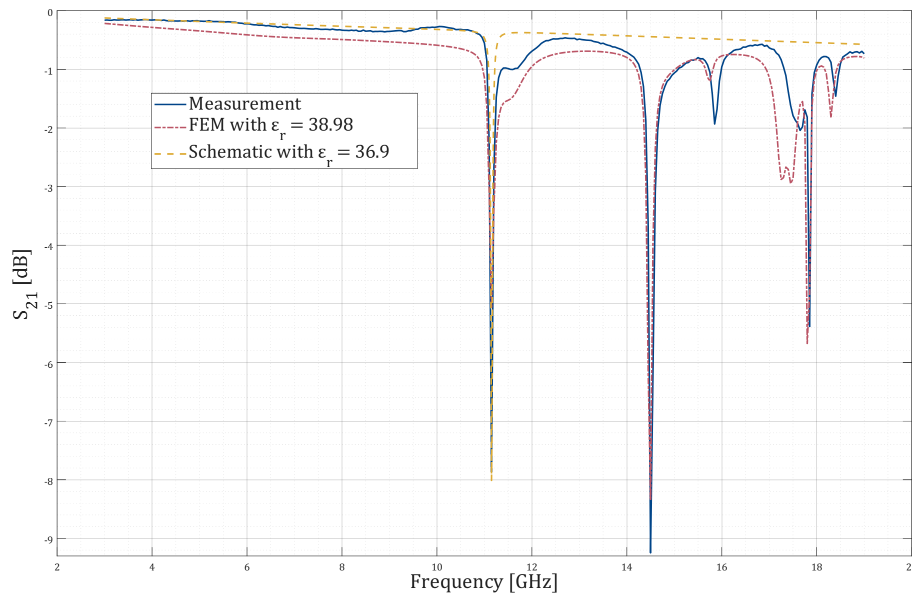

Figure 5.9: S_{21}-parameters from FEM and schematic simulations with relative permittivity tuned in order to resonate at 11.15 GHz.

The FEM simulation shows closer overall agreement with the measured S-parameters, as it is based on a full-wave solution that accounts for non-idealities of the microstrip structure. However, when focusing on the frequency region around the first resonance, the schematic model provides a closer match to the measured response, as illustrated in Figure 5.10. This suggests that while the full-wave model better captures the broadband behaviour of the structure, the schematic representation may more accurately reproduce the local resonant behaviour under simplified assumptions.

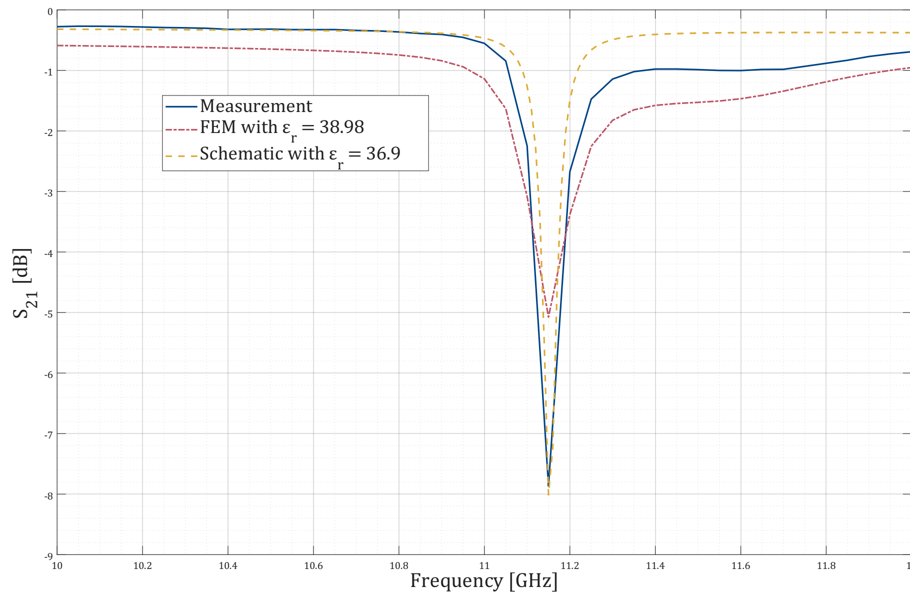

Figure 5.10: Close-up of the measured, schematic and FEM transmission around the first resonance frequency.

Using the S-parameters from the measurement as well as FEM and schematic simulations, we can compare the calculated coupling factor, β, and Q-factors calculated with the three-point method and the de-embeded characteristic impedance of the resonator. The result is shown in Table 5.2.

Table 5.2: Coupling factor and unloaded quality factor obtained using the three-point method (Algorithm 2) and from the phase of the de-embedded characteristic impedance of the resonator (Algorithm 3).

Method	**Coupling factor, β**	**Q_0 (three-point)**	**Q_0 (phase of Z)**
Measured	1.49	499.19	124.43
FEM simulation	0.62	88.03	81.28
Schematic simulation	1.33	841.53	384.76

A considerable discrepancy is observed between the quality factors obtained using the three-point method and those derived from the phase of the de-embedded resonator impedance for both the measured data and the schematic simulation. This difference could be due to strong coupling effects, where the assumptions underlying the impedance de-embedding procedure are no longer fully valid.

For the FEM simulation, the extracted quality factor is the lowest among the compared cases. This is also reflected in Figure 5.10, where the resonance dip exhibits the largest magnitude. These differences directly influence the extracted coupling coefficient, which may explain the lower value. These results suggest that the estimated relative permittivity depends on the chosen simulation model. In particular, the schematic model provides better agreement in the immediate vicinity of the

resonance, whereas the FEM model more accurately captures broadband behaviour and higher-order resonances.

To further asses if this method can be used to calculate the relative permittivity, we can evaluate how the numerical models perform with a resonator with the same dimensions as the commercial resonator.Varying the relative permittivity between 27 and 40, we can see how the resonance frequency changes in Figure 5.11. The specified permittivity and resonant frequency of the DRT 10.5 GHz resonator are included for reference.

Figure 5.11: Resonant frequency as a function of relative permittivity for a cylindrical resonator with a diameter of 5.07 mm and height of 2.19 mm, calculated using numerical methods presented by Pozar [21], Itoh and Rudokas [27], and Konishi *et al* [26]. The specified permittivity and resonance frequency of the DRT 10.5 GHz resonator is also plotted.

Using the transcendental model by Pozar [21], a relative permittivity of $\varepsilon_r = 27.8$ is required to obtain a resonant frequency of 11.15 GHz for a resonator with the same dimensions as the DRT 10.5 GHz. In comparison, the model by Itoh and Rudokas [27] yields an estimated permittivity of approximately 40, while the formulation by Konishi *et al.* [26] results in a value below 20. This highlights the need for complementary measurement techniques to more accurately determine the relative permittivity.

5.3 Multiline method

Using the multiline method, the relative permittivity and loss tangent calculated from S-parameter measurements from two microstrip lines with a length difference of 4.14 mm were compared to calculations using S-parameters from simulations using the schematic layout in ADS. For both simulation methods, input parameters included ε_r and $\tan\delta$ which were set according to the data sheet of the I-Tera MT40 substrate as $\varepsilon_r = 3.38$ and $\tan\delta = 0.0028$ at 10 GHz. The result at 10 GHz is summarised in Table 5.3 for the measured and simulated result, and compared to the values presented in the data sheet for the substrate.

Table 5.3: Relative permittivity and loss tangent at 10 GHz from measurements and simulations compared to data sheet values for I-Tera MT40.

	Relative permittivity, ε_r	**Loss tangent,** $\tan\delta$
Data sheet	3.38-3.75	0.0028-0.0035
Measured	3.31	0.0039
Schematic simulation	3.43	0.0031

The relative permittivity and loss tangent from 3 GHz to 19 GHz is presented in Figure 5.12. The results using measured and simulated S-parameters are quite similar,

indicating that this is a valid method for calculating the dielectric properties.

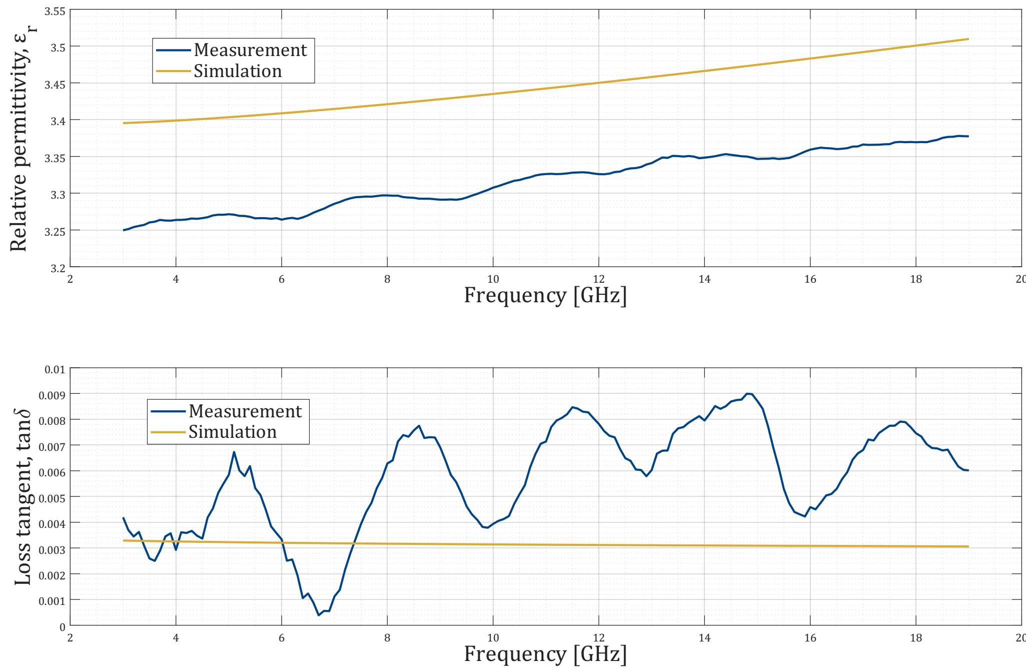

Figure 5.12: Relative permittivity and loss tangent calculated using the multiline method from measured and simulated S-parameters from two microstrip lines with a length difference of 4.14 mm. The dielectric loss was estimated taking conductor losses into account, but not accounting for surface roughness.

For the loss tangent, we can clearly see a wave-like pattern from the measurement. This is probably due to connector mismatch, which introduces a standing wave that can be seen in the S-parameters of the independent line measurements. The reason for this standing wave could be because the designed TRL kit did not have a metal plate for support. This made it hard to connect and disconnect to the SMA contacts without the PCB bending, which could account for the perturbations. In the multiline method, the main assumption is that the non-idealities are the same for both lines. If this is not the case, there is the possibility of small perturbations having a large impact on the derived quantities. Differences in how the lines are connected could have an impact for example, even if this difference is miniscule. As the loss tangent values are small in themselves, the impact is more noticeable. However, from simulations we can conclude that the multiline method does give accurate results in terms of relative permittivity and loss tangent. If time was spent on minimising connector and impedance mismatch, the result could be very accurate. Using the S-parameters from the schematic simulation, the calculated parameters are close to the input with a less than 2 percent difference in the relative permittivity and around 10 percent difference in loss tangent.

As a next step, a 3D printed ceramic substrate could be fabricated and plated with gold or copper in order to form two microstrip lines and a ground plane. This would give accurate broadband measurement results, and would also be easy to implement if multi-material printing with metal and ceramic is available. The

dielectric properties also fall out directly from equations without having to use numerical approximations or electromagnetic simulations, and are not limited to a specific set of frequencies. More investigation is needed for this method, in order to determine its limitation. This could be done with schematic simulations in ADS, which are quick to perform.

6
Conclusion

The aim of this Master's thesis was to develop and propose characterisation methods for the dielectric properties of additively manufactured materials, in particular relative permittivity and loss tangent. In addition, the influence of different stages of the fabrication process on these properties was evaluated. To achieve this, three dielectric characterisation methods were developed and investigated. The first method employed 3D-printed ceramic cubes configured as parallel-plate capacitors to determine both relative permittivity and loss tangent. The second method utilised a dielectric resonator coupled to a microstrip line for loss tangent extraction, while the third method was based on broadband S-parameter measurements of transmission lines with a known length difference to determine both relative permittivity and loss tangent. Of these methods, the parallel-plate capacitor approach was applied to characterise the material throughout the complete manufacturing process, including the green body, sintered, and hot isostatically pressed (HIPed) states.

The results demonstrate a strong dependence of dielectric performance on material density. An increase in density of 0.6% resulted in a 31.4% increase in relative permittivity and a 15.4% reduction in loss tangent. These findings are consistent with previous studies that have identified porosity as a critical factor governing the dielectric behaviour of ceramic materials. Furthermore, the temperature dependence of the dielectric properties was investigated between 25 °C and 100 °C. Over this temperature range, the relative permittivity remained comparatively stable, varying by less than 2%, whereas the loss tangent increased by approximately 250%, indicating that dielectric losses are considerably more sensitive to temperature than permittivity.

The measured dielectric properties of both sintered and HIPed samples did not meet the values specified by the material manufacturer. This discrepancy suggests that dielectric performance is highly sensitive to processing conditions and that material density alone does not fully explain the observed behaviour. In particular, the results indicate that the sintering stage plays a critical role in determining the final dielectric properties. As microstructural characterisation was outside the scope of this work, the relationship between dielectric performance and microstructural features such as grain size, residual porosity, and grain-boundary characteristics could not be directly assessed. Future investigations combining dielectric measurements with microstructural analysis would therefore provide valuable insight into the mechanisms governing the observed material behaviour.

Several limitations should be acknowledged. The number of characterised samples

was limited, and only one of the three proposed measurement methods was applied to all fabrication stages. Consequently, a comprehensive comparison between the different characterisation techniques could not be performed. Nevertheless, the results provide meaningful insight into the influence of additive manufacturing and post-processing on dielectric properties and contribute to the growing body of knowledge on additively manufactured microwave ceramics. Furthermore, the thesis demonstrates three practical and accessible measurement approaches that can be implemented for rapid dielectric assessment and process evaluation.

Future work should focus on establishing clearer relationships between processing parameters, microstructure, and dielectric performance. In particular, the influence of sintering temperature, sintering duration, layer thickness, and other manufacturing parameters should be systematically investigated. Additional measurements using the resonator-based and transmission-line-based methods would also enable validation of the parallel-plate capacitor results and facilitate an assessment of the accuracy, repeatability, and frequency-dependent performance of the different techniques. Overall, the findings demonstrate that achieving dielectric properties comparable to those of conventionally manufactured ceramics requires careful optimisation of all stages of the additive manufacturing process, from printing and debinding to sintering and post-processing.

Bibliography

[1] D. Misra, "Evolution of dielectric Science and Technology for nanoelectronics," *The Electrochemical Society Interface*, vol. 20, no. 4, pp. 31–31, 2011.

[2] R. L. Opila and D. W. Hess, "A Century of Dielectric Science and Technology," *Journal of The Electrochemical Society*, vol. 150, no. 1, S1, Dec. 2002. DOI: 10.1149/1.1529671. [Online]. Available: https://doi.org/10.1149/1.1529671.

[3] P. Nayeri et al., "3D Printed Dielectric Reflectarrays: Low-Cost High-Gain Antennas at Sub-Millimeter Waves," *IEEE Transactions on Antennas and Propagation*, vol. 62, no. 4, pp. 2000–2008, 2014. DOI: 10.1109/TAP.2014.2303195.

[4] G. P. Le Sage, "3D Printed Waveguide Slot Array Antennas," *IEEE Access*, vol. 4, pp. 1258–1265, 2016. DOI: 10.1109/ACCESS.2016.2544278.

[5] D. Miek et al., "Ceramic Additive Manufactured Monolithic X-Shaped TM Dual-Mode Filter," *IEEE Journal of Microwaves*, vol. 2, no. 3, pp. 496–506, 2022. DOI: 10.1109/JMW.2022.3167250.

[6] C. Guo, X. Shang, M. J. Lancaster, and J. Xu, "A 3-D Printed Lightweight X-Band Waveguide Filter Based on Spherical Resonators," *IEEE Microwave and Wireless Components Letters*, vol. 25, no. 7, pp. 442–444, 2015. DOI: 10.1109/LMWC.2015.2427653.

[7] M. Bai, Y. Zhang, J. Xu, L. Hu, and J. Hu, "A 3D Printed X-Band Waveguide Filter Based on Bowtie-Shaped Resonator," in *2023 International Conference on Microwave and Millimeter Wave Technology (ICMMT)*, 2023, pp. 1–3. DOI: 10.1109/ICMMT58241.2023.10276391.

[8] D. Miek, S. Simmich, F. Kamrath, and M. Höft, "Additive Manufacturing of E-Plane Cut Dual-Mode X-Band Waveguide Filters With Mixed Topologies," *IEEE Transactions on Microwave Theory and Techniques*, vol. 68, no. 6, pp. 2097–2107, 2020. DOI: 10.1109/TMTT.2020.2981057.

[9] P. Booth and E. V. Lluch, "Enhancing the Performance of Waveguide Filters Using Additive Manufacturing," *Proceedings of the IEEE*, vol. 105, no. 4, pp. 613–619, Apr. 2017.

[10] C. Bartlett, D. Miek, F. Kamrath, D. Bruhn, and M. Höft, "X-Band 3D-Printed Metal-Insert Twist-Component for Bandpass Filter Applications," in *2021 IEEE MTT-S International Microwave Filter Workshop (IMFW)*, 2021, pp. 329–331. DOI: 10.1109/IMFW49589.2021.9642300.

[11] M. Baranowski, L. Balewski, A. Lamecki, and M. Mrozowski, "Low-Loss 3D-Printed Waveguide Filters Based on Deformed Dual-Mode Cavity Resonators," *IEEE Access*, vol. 12, pp. 78 275–78 285, 2024. DOI: 10.1109/ACCESS.2024.3408671.

[12] A. Pons-Abenza et al., "Rigorous Design of Compact High-Performance 3-D Microstrip Filters Using Inverse Scattering," *IEEE Microwave and Wireless Technology Letters*, vol. 35, no. 12, pp. 1913–1916, 2025. DOI: 10.1109/LMWT.2025.3605549.

[13] P. Boe, D. Brouczek, L. Mikiss, M. Hofbauer, D. Miek, and M. Höft, "Compact Ku-Band Diplexer With Additive Manufactured Multimaterial Dielectric Resonator Insets," *IEEE Microwave and Wireless Technology Letters*, vol. 35, no. 6, pp. 800–803, 2025. DOI: 10.1109/LMWT.2025.3562691.

[14] P. Vallerotonda, L. Pelliccia, F. Cacciamani, C. Tomassoni, and O. Bouzekri, "Additive-Manufactured $TM_{01\delta}$ Mode Dielectric Resonators for Compact On-Board Wideband Filters," in *2023 53rd European Microwave Conference (EuMC)*, 2023, pp. 388–391. DOI: 10.23919/EuMC58039.2023.10290540.

[15] J. Deckers, J. Vleugels, and J.-P. Kruth, "Additive manufacturing of ceramics: A review," *J. Ceram. Sci. Technol*, vol. 5, no. 4, pp. 245–260, 2014. DOI: 10.4416/JCST2014-00032.

[16] P. I. Deffenbaugh, R. C. Rumpf, and K. H. Church, "Broadband Microwave Frequency Characterization of 3-D Printed Materials," *IEEE Transactions on Components, Packaging and Manufacturing Technology*, vol. 3, no. 12, pp. 2147–2155, Dec. 2013. DOI: 10.1109/tcpmt.2013.2273306.

[17] A. A. Takach, F. M. Moukanda, F. Ndagijimana, M. Al-Husseini, and J. Jomaah, "Two-Line Technique for Dielectric Material Characterization with Application in 3D-Printing Filament Electrical Parameters Extraction," *Progress In Electromagnetics Research M*, vol. 85, pp. 195–207, 2019. DOI: 10.2528/pierm19071702.

[18] A. Goulas et al., "The Impact of 3D Printing Process Parameters on the Dielectric Properties of High Permittivity Composites," *Designs*, vol. 3, no. 4, p. 50, Nov. 2019. DOI: 10.3390/designs3040050.

[19] F. Castles et al., "Microwave dielectric characterisation of 3D-printed $BaTiO_3$/ABS polymer composites," *Scientific reports*, vol. 6, no. 1, p. 22 714, 2016. DOI: 10.1038/srep22714.

[20] A. Alimenti, K. Torokhtii, N. Pompeo, E. Piuzzi, and E. Silva, "Characterisation of dielectric 3D-printing materials at microwave frequencies," *Acta Imeko*, vol. 9, no. 3, pp. 26–32, 2020. DOI: 10.21014/acta_imeko.v9i3.778.

[21] D. M. Pozar, *Microwave Engineering*, 4th ed. Hoboken, NJ: Wiley, 2021, ISBN: 978-1-119-77061-9.

[22] R. D. Richtmyer, “Dielectric Resonators,” *Journal of Applied Physics*, vol. 10, no. 6, pp. 391–398, Jun. 1939, ISSN: 0021-8979. DOI: 10.1063/1.1707320. eprint: https://pubs.aip.org/aip/jap/article-pdf/10/6/391/18304271/391_1_online.pdf. [Online]. Available: https://doi.org/10.1063/1.1707320.

[23] M. Pospieszalski, “Cylindrical Dielectric Resonators and Their Applications in TEM Line Microwave Circuits,” *IEEE Transactions on Microwave Theory and Techniques*, vol. 27, no. 3, pp. 233–238, 1979. DOI: 10.1109/TMTT.1979.1129599.

[24] S. Cohn, “Microwave Bandpass Filters Containing High-Q Dielectric Resonators,” *IEEE Transactions on Microwave Theory and Techniques*, vol. 16, no. 4, pp. 218–227, 1968. DOI: 10.1109/TMTT.1968.1126654.

[25] J. Sethares and S. Naumann, “Design of Microwave Dielectric Resonators,” *IEEE Transactions on Microwave Theory and Techniques*, vol. 14, no. 1, pp. 2–7, 1966. DOI: 10.1109/TMTT.1966.1126144.

[26] Y. Konishi, N. Hoshino, and Y. Utsumi, “Resonant Frequency of a $TE_{01\delta}$° Dielectric Resonator,” *IEEE Transactions on Microwave Theory and Techniques*, vol. 24, no. 2, pp. 112–114, 1976. DOI: 10.1109/TMTT.1976.1128783.

[27] T. Itoh and R. Rudokas, “New Method for Computing the Resonant Frequencies of Dielectric Resonators (Short Papers),” *IEEE Transactions on Microwave Theory and Techniques*, vol. 25, no. 1, pp. 52–54, 1977. DOI: 10.1109/TMTT.1977.1129030.

[28] R. Freer and F. Azough, “Microstructural engineering of microwave dielectric ceramics,” *Journal of the European Ceramic Society*, vol. 28, no. 7, pp. 1433–1441, 2008, ISSN: 0955-2219. DOI: https://doi.org/10.1016/j.jeurceramsoc.2007.12.005.

[29] S. J. Penn et al., “Effect of Porosity and Grain Size on the Microwave Dielectric Properties of Sintered Alumina,” *Journal of the American Ceramic Society*, vol. 80, no. 7, pp. 1885–1888, 1997. DOI: https://doi.org/10.1111/j.1151-2916.1997.tb03066.x.

[30] K.-D. Jenkel et al., “Effect of sintering temperature on the dielectric properties of 3D-printed alumina (Al2O3) in the W-band,” *Journal of the American Ceramic Society*, vol. 107, no. 4, pp. 2494–2503, 2024. DOI: https://doi.org/10.1111/jace.19597.

[31] P. Denisowski. “VNA calibration methods and standards,” Accessed: May 19, 2026. [Online]. Available: https://www.rohde-schwarz.com/us/products/test-and-measurement/essentials-test-equipment/spectrum-analyzers/vna-calibration-methods-and-standards_258187.html.

[32] “TRL Calibration,” Accessed: May 19, 2026. [Online]. Available: https://helpfiles.keysight.com/csg/pxivna/S3_Cals/TRL_Calibration.htm.

[33] Keysight Technologies, *Impedance Measurement Handbook*, 6th Edition, Keysight Technologies, 1400 Fountaingrove Parkway, Santa Rosa, CA 95403. Accessed: Apr. 27, 2026. [Online]. Available: https://www.keysight.com/us/en/assets/7018-06840/application-notes/5950-3000.pdf.

[34] C. J. Kaiser, *The Capacitor Handbook*, 2012. DOI: 10.1007/978-94-011-8090-0. Accessed: Apr. 27, 2026.

[35] A. Khanna and Y. Garault, "Determination of loaded, unloaded, and external quality factors of a dielectric resonator coupled to a microstrip line," *IEEE Transactions on Microwave Theory and Techniques*, vol. 31, no. 3, pp. 261–264, 2003. DOI: 10.1109/TMTT.1983.1131473.

[36] W. Wheless, "A resonator impedance de-embedding procedure," *IEEE Transactions on Instrumentation and Measurement*, vol. 38, no. 4, pp. 864–869, 1989. DOI: 10.1109/19.31005.

[37] R. Marks, "A multiline method of network analyzer calibration," *IEEE Transactions on Microwave Theory and Techniques*, vol. 39, no. 7, pp. 1205–1215, 1991. DOI: 10.1109/22.85388.

[38] M. Janezic and J. Jargon, "Complex permittivity determination from propagation constant measurements," *IEEE Microwave and Guided Wave Letters*, vol. 9, no. 2, pp. 76–78, 1999. DOI: 10.1109/75.755052.

[39] E. Hammerstad and O. Jensen, "Accurate Models for Microstrip Computer-Aided Design," in *1980 IEEE MTT-S International Microwave symposium Digest*, 1980, pp. 407–409. DOI: 10.1109/MWSYM.1980.1124303.

[40] D. C. DeGroot, D. K. Walker, and R. B. Marks, "Impedance mismatch effects on propagation constant measurements," in *Proc. 1996 IEEE Conf. Packag*, 1996, pp. 141–143.

[41] Y. Rolain, W. Van Moer, J. A. Jargon, and D. C. DeGroot, "On Peculiarities of *S*-Parameter Measurements," *IEEE Transactions on Instrumentation and Measurement*, vol. 56, no. 5, pp. 1967–1972, 2007. DOI: 10.1109/TIM.2007.895581.

[42] W. Tang et al., "Materials and underlying principles in vat photopolymerization-based additive manufacturing of electronic ceramics," *Progress in Materials Science*, vol. 154, p. 101 498, 2025. DOI: https://doi.org/10.1016/j.pmatsci.2025.101498.

[43] "CeraFab Multi 2M30 The Multimaterial 3D Printer," Accessed: May 25, 2026. [Online]. Available: https://www.lithoz.com/en/3d-printer/cerafab-multi/.

[44] S. Allan, P. Schneider, D. Bomze, I. Potestio, M. Schwentenwein, and J. Homa, "Lithography-Based Ceramic Manufacturing," *Ceramic Industry*, vol. 167, no. 5, pp. 16–19, May 2017, ISSN: 0009-0220.

[45] "LCM Technology: How to 3D Print Ceramics," Accessed: May 22, 2026. [Online]. Available: https://www.lithoz.com/en/technology/lcm-technology/.

[46] E. Schwarzer, M. Götz, D. Markova, D. Stafford, U. Scheithauer, and T. Moritz, “Lithography-based ceramic manufacturing (LCM) – Viscosity and cleaning as two quality influencing steps in the process chain of printing green parts,” *Journal of the European Ceramic Society*, vol. 37, no. 16, pp. 5329–5338, 2017, Shaping of Advanced Ceramics, ISSN: 0955-2219. DOI: https://doi.org/10.1016/j.jeurceramsoc.2017.05.046. [Online]. Available: https://www.sciencedirect.com/science/article/pii/S0955221917303990.

[47] “Material Overview LCM Technology,” Accessed: May 22, 2026. [Online]. Available: https://www.lithoz.com/wp-content/uploads/2025/11/Lithoz_Materialfolder_EN_Digital.pdf.

[48] “What is Hot Isostatic Pressing (HIP)?” Accessed: May 22, 2026. [Online]. Available: https://quintustechnologies.com/faq/what-is-hot-isostatic-pressing-hip/.

DEPARTMENT OF MICROTECHNOLOGY AND NANOSCIENCE
CHALMERS UNIVERSITY OF TECHNOLOGY
Gothenburg, Sweden
www.chalmers.se

CHALMERS
UNIVERSITY OF TECHNOLOGY